Title

Presynaptic NMDA receptors cooperate with local action potentials to implement activity-dependent GABA release from the reciprocal olfactory bulb granule cell spine

Authors

Vanessa Lage-Rupprecht[1,2], Li Zhou[1], Gaia Bianchini[1], S. Sara Aghvami[1,3,4], Balázs Rózsa[5], Marco Sassoé-Pognetto[6] & Veronica Egger[1*]

Affiliations

1. Neurophysiology, Institute of Zoology, Universität Regensburg, 93040 Regensburg, Germany; 2. Department of Bioinformatics, Fraunhofer SCAI, 53757 Sankt Augustin, Germany; 3. School of Electrical and Computer Engineering, University of Tehran, 14395-515 Tehran, Iran; 4. School of Cognitive Sciences, Institute for Research in Fundamental Sciences (IPM), 19395-5746 Tehran, Iran; 5. Two-Photon Imaging Center, Institute of Experimental Medicine, Hungarian Academy of Sciences, 1039 Budapest, Hungary; 6. Neuroscience Department, University of Turin, I-10126 Torino, Italy.

Abstract

In the rodent olfactory bulb the smooth dendrites of the principal glutamatergic mitral cells (MCs) form reciprocal dendrodendritic synapses with large spines on GABAergic granule cells (GC), where unitary release of glutamate can trigger postsynaptic local activation of voltage-gated Na^+-channels (Na_vs), i.e. a spine spike. Can such single MC inputs evoke reciprocal release? We find that unitary-like activation via two-photon uncaging of glutamate causes GC spines to release GABA both synchronously and asynchronously onto MC dendrites. This release indeed requires activation of Na_vs and high-voltage-activated Ca^{2+}-channels (HVACCs), but also of NMDA receptors (NMDAR). Simulations show temporally overlapping HVACC- and NMDAR-mediated Ca^{2+}-currents during the spine spike, and ultrastructural data prove NMDAR presence within the GABAergic presynapse. The cooperative action of presynaptic NMDARs allows to implement synapse-specific, activity-dependent and non-topographical lateral inhibition and thus could provide an efficient solution to combinatorial percept synthesis in a sensory system with many receptor channels.

Introduction

Reciprocal dendrodendritic microcircuits can be found in several parts of the nervous system and are especially abundant in the vertebrate olfactory bulb (*Crespo et al. 2013*), where the dendrites of the principal mitral and tufted cells (MTCs) engage in such interactions with several major subtypes of local GABAergic neurons. In the glomerular layer, the MTC apical tuft is reciprocally connected to mostly periglomerular cell dendrites. In the external plexiform layer, the long MC lateral dendrites are densely covered with GABAergic synapses that mostly originate from reciprocal arrangements (*Bartel et al. 2015; Sailor et al. 2016; Matsuno et al. 2017*). While proximal circuits are thought to be mostly formed by granule cell (GC) spines (*Miyamichi et al. 2013*), there are also reciprocal dendrodendritic interactions with other GABAergic cell types such as SOM+ neurons, CRH+ neurons and most prominently parvalbumin/PV+ neurons that all feature aspiny, smooth dendrites (partially overlapping populations; *Toida et al. 1994; Lepousez et al. 2010; Huang et al. 2013; Kato et al. 2013; Miyamichi et al. 2013)*.

Thus the MC-GC synapse differs from the other bulbar reciprocal arrangements by its location within a large spine on the GC side. These spines feature particularly long necks (*Woolf et al. 1991*) which might serve to electrically isolate the synapse and boost local

processing (e.g. *Miller et al. 1985; Spruston 2008*). Indeed, we have gathered evidence that unitary postsynaptic potentials in GC spines are electrically compartmentalized and thus can locally activate voltage-gated Na^+-channels (Na_vs) which in turn activate classic presynaptic high-voltage activated Ca^{2+}-channels (HVACCs) within the spine ('spine spike', *Bywalez et al. 2015*). Thus, the reciprocal spine might operate as a mini-neuron that can generate synaptic output upon local activation (*Egger & Urban 2006*).

While there have been many earlier studies of recurrent dendrodendritic inhibition at the MTC-GC synapse, it is so far unknown whether a unitary, purely local activation of the spine's microcircuit can indeed trigger release of GABA back onto the exciting MTC. The issue is still unresolved because (1) paired recordings of synaptically coupled GCs and MTCs are notoriously hard to perform (e.g. *Pressler & Strowbridge 2017;* see also Discussion) and would also not allow to fully dissect the circuit, and (2) most earlier studies used a strong stimulation of voltage-clamped MCs, namely a depolarization to 0 mV for 20-50 ms *(Isaacson & Strowbridge 1998; Halabisky et al. 2000; Isaacson 2001; Chen et al. 2000*). This protocol will cause massive release of glutamate from the lateral MC dendrites, invoking glutamate spillover between them (*Isaacson 1999*) and resulting in long-lasting recurrent inhibition of MCs with both synchronous and asynchronous components, the latter with a time constant of ~ 500 ms. Under these circumstances and zero extracellular $[Mg^{2+}]_e$ GC NMDA receptor (NMDAR) activation was shown to be an important source of Ca^{2+} entry that suffices to trigger release of GABA from the GC spine (also in *Schoppa et al. 1998*). However, in normal $[Mg^{2+}]_e$ GABA release was mostly abolished by HVACC blockade (*Isaacson 2001*; see Discussion).

Here we aim to determine whether – and possibly how - single inputs from MC lateral dendrites to GC spines can also trigger recurrent release of GABA from the reciprocal synapse, using recordings from fluorescently labeled MCs and two-photon uncaging (TPU) of glutamate along their lateral dendrite near Venus-tagged GC spines. TPU of glutamate allows to study the activation of the reciprocal microcircuit in single GC spines without interfering with spine Na_v and HVACC channels or causing broader GC activation (*Bywalez et al. 2015*), which here also enables investigation of the reciprocal output by the GABAergic release machinery via recording of IPSCs in mitral cells in response to TPU at single GC

78 spines. Thus, processing within a single mini-neuron can be disentangled in space and time
79 from broader extended activation, in order to test the main predictions from our previous
80 study: The mini-neuron hypothesis along with the GC spine spike phenomenon suggest that
81 just like in conventional axons, Na_v and ensuing HVACC activation are required to cause
82 release, and that unitary activation of the spine is sufficient for triggering release.
83 While these notions could be confirmed, our study also reveals that presynaptic NMDARs
84 can gate reciprocal output at the single-spine level. What is the advantage of such an
85 arrangement compared to classical neuronal processing? In olfactory coding, a large number
86 of input channels needs to be combined to synthesize an olfactory percept (e.g. *Mori et al.*
87 *1999, Murthy 2011*). We propose that the mechanisms revealed here allow reciprocal GC
88 spines to play a central role in the efficient binding of changing sets of activated olfactory
89 receptor channels.
90
91 ***Results***
92 *Experimental configuration*
93 To enable pharmacological interference with components of the reciprocal microcircuit such
94 as Na_vs and HVACCs, we bypassed release from the MC presynapse via TPU of DNI-caged
95 glutamate (DNI, see Methods; *Chiovini et al. 2014; Bywalez et al. 2015; Palfi et al. 2018*) in
96 acute juvenile rat olfactory bulb slices, while recording from MCs in somatic whole-cell
97 voltage-clamp. To visualize the lateral dendrites, MCs were filled with the dye Alexa594 (50
98 μM). Fig. 1A shows the recording configuration.
99 In all MC recordings we observed a high basal frequency of spontaneous events which is a
100 general hallmark of the olfactory bulb network *(Egger & Urban 2006*). Wash-in of 1 mM DNI
101 further increased the basal frequency by on average 1.9 ± 1.2 times (mean value before DNI:
102 4.5 ± 2.1 Hz, n = 14, $P < 0.01$), due to the disinhibition resulting from a partial blockade of
103 $GABA_A$Rs by DNI, which also reduced the mean spontaneous IPSC amplitude to a fraction of
104 0.47 ± 0.16 of control (n = 14 MCs, $P < 0.001$, Fig. S1A,B,C (attached at the end of the
105 manuscript). In the presence of DNI, the $GABA_A$R antagonist bicuculline (BCC, 50 μM)
106 blocked spontaneous activity almost completely (frequency: 0.13 ± 0.10 of control, n = 6, $P <$
107 0.01, Fig. 1C, Fig. S1A).

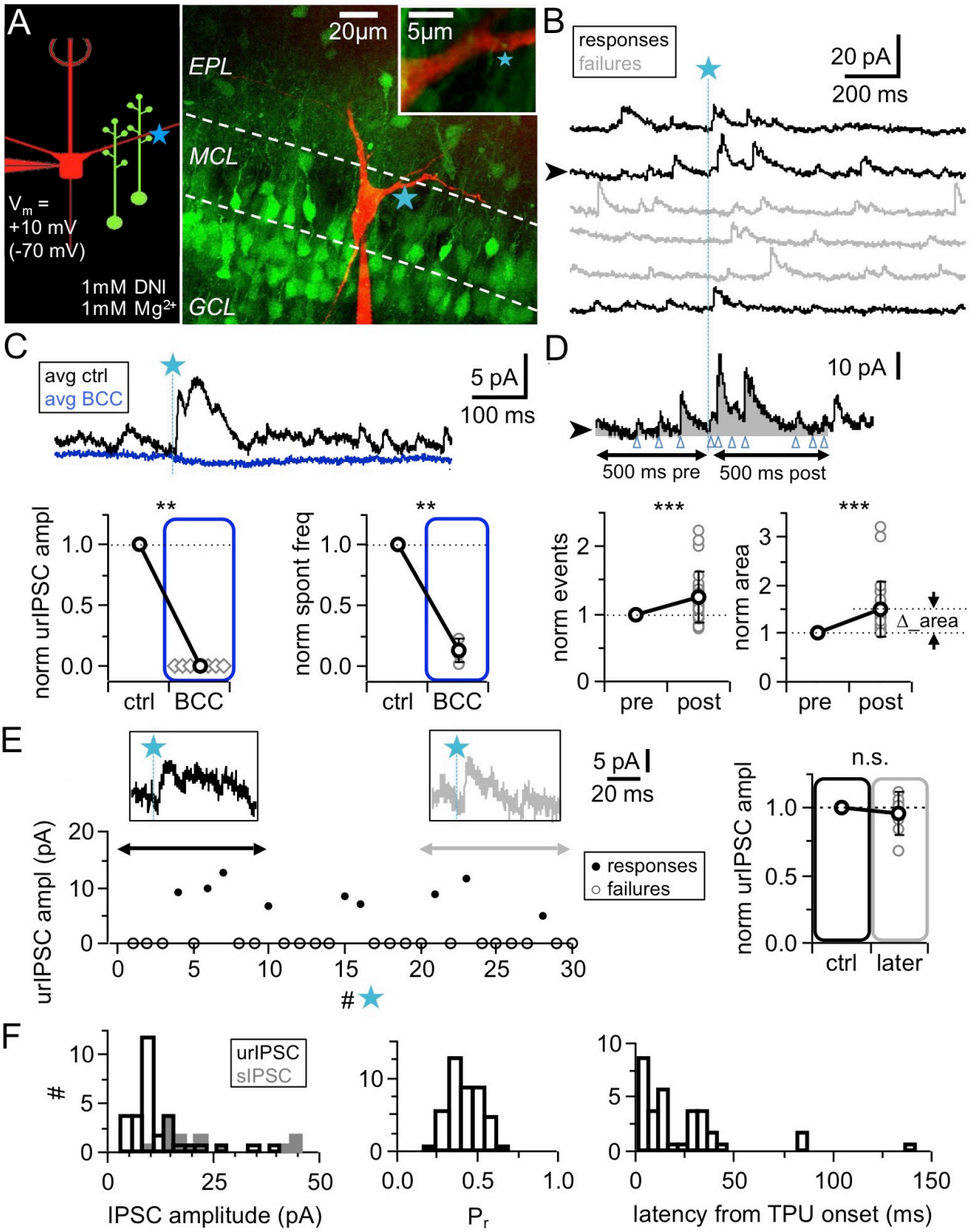

Figure 1. **TPU-induced glutamatergic activation of GC spines triggers GABA release detected as uncaging-evoked reciprocal IPSCs (urIPSCs) in MCs.**

(**A**) Experimental setting (scheme and image): Somatic whole cell voltage clamp recording from MC filled with Alexa 594 (red, 50 µM) and TPU of DNI-caged glutamate (DNI; blue star) at GC spines in VGAT-Venus rats (GCs green).

(**B**) Example of consecutive uncaging traces showing urIPSC responses (black) and failures (grey).

(**C**) Effect of $GABA_AR$ blockade (bicuculline, BCC, 50 µM, blue) on urIPSCs and spontaneous activity. Top: Example experiment, showing averaged traces. Bottom: Cumulative data on urIPSC amplitude (left panel, n =7) and on frequency of spontaneous events (right panel, n = 6).

(D) Analysis of asynchronous events. Top: Example trace from (B) with analysis intervals pre- and post-uncaging (grey areas, black arrows). Counted events marked by blue arrowheads. Bottom: Normalized IPSC event number and area (integrated activity, relative increase vs control Δ) in pre- versus post-uncaging intervals (n = 27, see Methods).

(**E**) Stability of urIPSC recordings. Left: Representative experiment showing individual urIPSC amplitude values over consecutive stimulations (1 TPU per min). Insets: Averaged urIPSC responses in the first (black, n = 3 responses) and last ten minutes (grey, n = 3). Right: Comparison of averaged normalized urIPSC amplitudes separated by 10 min interval (n = 7 MCs).
(**F**) Properties of first triggered urIPSCs. Left: Amplitudes (n = 32 MCs, V_m = +10 mV). Dark grey: Amplitude distribution of spontaneous IPSCs for comparison (n = 14 MCs, mean amplitudes). Middle: Release probabilities P_r (n = 44). Right: Latencies from TPU onset (n = 36).
All Figures: Significance (non-parametric tests): n.s. not significant, * $P < 0.05$, ** $P < 0.01$, *** $P < 0.001$; mean data ± S.D.

Since in initial experiments we occasionally observed activation of both NMDA and AMPA autoreceptors on MC dendrites at a holding potential of -70 mV, MCs were clamped to +10 mV in the main body of experiments, near the reversal potential of ionotropic glutamate receptors (*Isaacson 1999; Friedman & Strowbridge 2000*). All experiments were performed at physiological levels of $[Mg^{2+}]_e$ (1 mM).

Triggering of reciprocal IPSCs via TPU

To prevent overstimulation with glutamate, we uncaged with similar laser parameter settings as in the previous study (*Bywalez et al. 2015*), in which TPU-evoked GC Ca^{2+} signals were indistinguishable from those of unitary spontaneous or triggered synaptic inputs, and routinely tested these settings; to ensure similar laser power across experiments, uncaging sites were located at a shallow depth no more than 20 – 30 µm below the surface of the tissue (see Methods). In most experiments, uncaging was performed at one spot in the immediate vicinity of GC spines that were visible in VGAT-Venus rats and in close proximity (0.2 – 0.5 µm) to the MC lateral dendrite (e.g. Fig. 1A, 2A); in a few initial experiments in WT rats uncaging was performed 'blindly' at up to four spots along the dendrite to increase the likelihood for triggering a unitary response (e.g. Fig. 2B; 18% of experiments, see Methods). Responses were detectable in ~ 30% of tested MCs (total n = 166, see Methods) and in this fraction of MCs would occur only in a small subset of stimulations (see below, Fig. 1F), thus overstimulation of the circuit appears unlikely. All uncaging spots were located proximally, at distances < 50 µm from the MC soma (Fig. S1D). The rationale for this choice was to minimize electrotonic attenuation, since IPSC amplitudes were already small (see above, Fig. S1A,C). Moreover, proximal stimulation and the use of VGAT-Venus rats should prevent inadvertent stimulation of reciprocal synapses with other interneuron types (see Introduction).

155 TPU of glutamate resulted in consecutive triggered responses and failures in MCs (Fig. 1B).
156 Responses were classified as triggered if they were observed repeatedly within the same
157 time window and showed similar kinetics (see Methods). Next we tested whether these
158 triggered responses were indeed GABAergic by applying the $GABA_AR$ antagonist Bicuculline
159 (BCC, 50 µM), which invariably blocked responses completely (Fig. 1C, n = 7, P < 0.01,
160 Wilcoxon test). Thus in the following the triggered events are denoted as urIPSCs (**u**ncaging-
161 evoked **r**eciprocal IPSCs). Sufficient stability of such urIPSC responses was established via
162 long-term recordings (see Methods). The mean amplitudes of responses during the first and
163 last 5 -10 photostimulations (with at least 10 min in between to mimic the time course of
164 pharmacological manipulations) were not significantly different (Fig. 1E, n = 7, ratio last to
165 first 0.95 ± 0.15, P = 0.74).
166 The amplitude of triggered urIPSCs was on average 12 ± 8 pA, with a rise time of 6 ± 3 ms
167 (in n = 32 MCs clamped to +10 mV), which is significantly smaller than the mean amplitudes
168 of spontaneous IPSCs (n = 14; 22 ± 12 pA; P < 0.001, Mann-Whitney test, Fig. 1F). Since
169 spontaneous IPSCs are highly likely to also originate from the reciprocal MC-GC circuit (see
170 Discussion), this observation further argues against overstimulation with glutamate in our
171 experiment. There was no detectable correlation between the urIPSC amplitude and the
172 distance from the soma (n = 20, r = -0.07, Fig. S1D).
173 The average release probability from the reciprocal spine was estimated as P_r = 0.34 ± 0.11
174 (Fig. 1F, range 0.13 - 0.60, based on n = 44 MCs, see Methods and Discussion). The
175 latencies of urIPSPCs were not normally distributed (Fig. 1F), with a first peak within the first
176 10 ms post TPU onset (n = 13), a second peak around 30 ms (n = 19 within the range 10-50
177 ms) and a yet more delayed tail (n = 3, see Fig. S1F and Discussion).
178 In most experiments we detected putative asynchronous urIPSCs following the first triggered
179 event which were quantified via integral analysis and counting of events (Fig. 1D, see
180 Methods and Discussion). Both area and number of events increased highly significantly in
181 the 500 ms interval following TPU ('post') compared to the same interval right before ('pre';
182 mean increase of integrated activity ∆_area + 0.50 ± 0.55 relative to 'pre' value; mean
183 increase in event number + 0.25 ± 0.37 relative to 'pre' value; n = 27, P < 0.001 for both;
184 absolute values in 'pre' area 2.40 ± 1.83 pAs, event numbers 26.1 ± 14.9). ∆_area was also

185 significantly increased if the extra area of the synchronous urIPSC was subtracted ($P <$
186 0.005). The total duration of recurrent inhibition was on average 179 ± 137 ms (range 32 –
187 533 ms, n = 26, Fig. S1E). Thus, asynchronous recurrent inhibition can be already triggered
188 by single glutamatergic inputs.
189 From all these experiments we conclude that local, unitary-like TPU of glutamate can indeed
190 trigger both fast and slow reciprocal release of GABA, providing proof that the reciprocal
191 microcircuit can be activated by single synaptic inputs at physiological levels of Mg^{2+}.
192 mean data ± S.D.

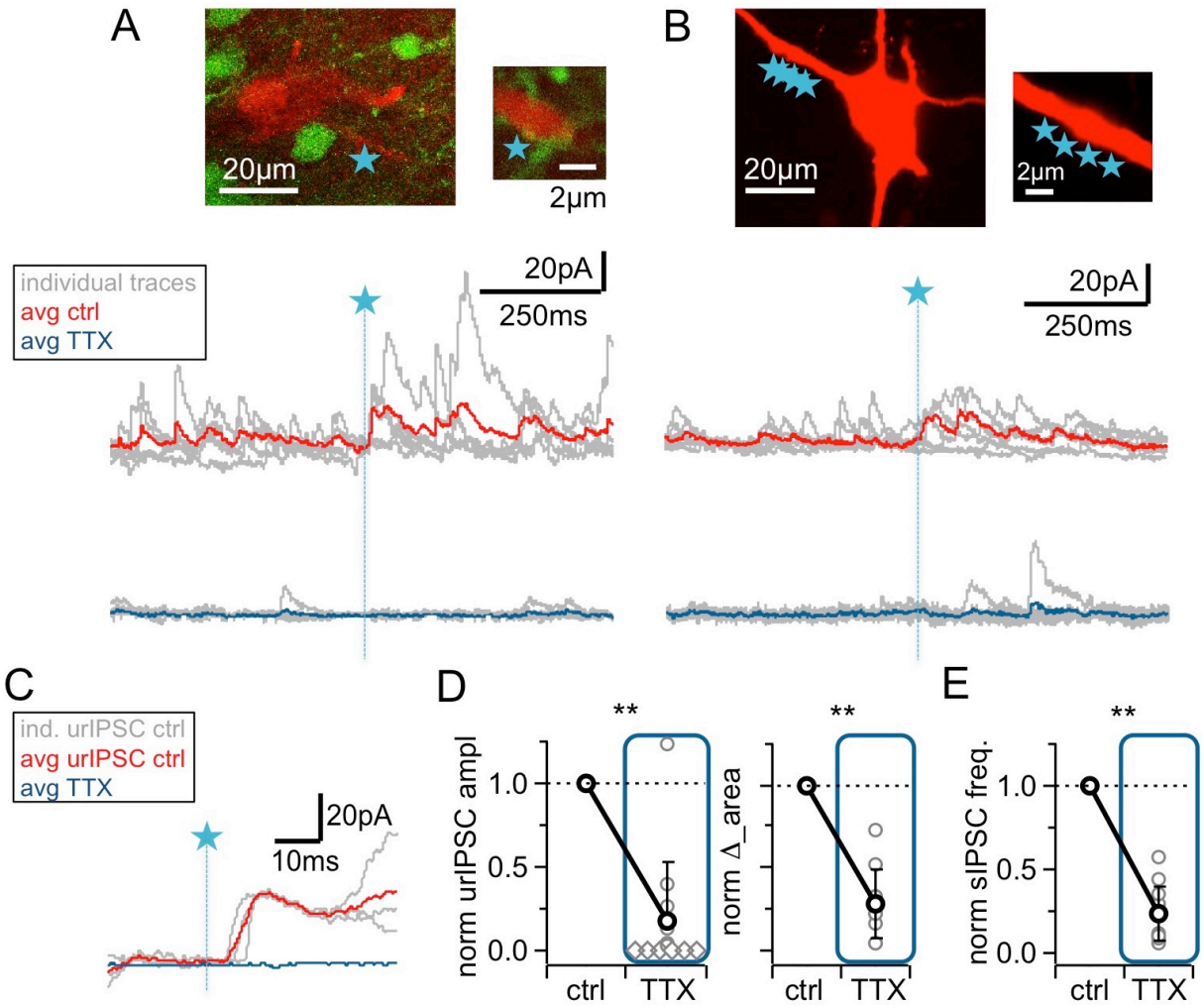

Figure 2. The urIPSC is reduced by Na_v blockade (TTX, 500 nM).
(**A, B**) Representative experiments showing a patch-clamped mitral cell (Alexa594 50 µM, red), the uncaging site(s) along a lateral dendrite (blue star) and below the corresponding uncaging traces with individual traces shown in grey, average control traces in red and average TTX traces indicated in blue (A: VGAT-Venus rat, single-site TPU, B: Wistar rat, multi-site TPU).
(**C**) Magnified illustration of traces in (A) (for control individual traces with urIPSC responses and their average, for TTX only average, color coding as above).
(**D**) Left: Cumulative normalized data showing the strong reduction of urIPSC amplitude during Na_v blockade with TTX (n = 12). Diamonds indicate the experiments with no detectable response in the presence of the drug. Right: Comparison of normalized IPSC Δ_area between control and in the presence of TTX (see Methods, n = 10).
(**E**) sIPSC frequency comparison beween control and in presence of TTX (n = 10). See also A,B.

Sodium channel activation is required for most urIPSCs

Next, we investigated a possible contribution of the GC spine spike and thus Na_v activation to urIPSC generation. Fig. 2 illustrates that wash-in of TTX (500 nM) substantially reduced both triggered and spontaneous events. On average, urIPSC amplitudes were reduced to a fraction of 0.17 ± 0.34 of control (Fig. 2D, n = 12, P < 0.005; absolute control amplitudes for -70 mV: -7.8 ± 3.6 pA, n = 5; for 10 mV: 15.4 ± 12.4 pA, n = 7), and the increase in integrated activity Δ_area was decreased to 0.28 ± 0.21 of its control value (see Methods; n = 10, P <

0.005). The frequency of spontaneous IPSCs (sIPSC) was also strongly decreased in TTX, to a fraction of 0.24 ± 0.17 of control (Fig. 2E, n = 10, P < 0.005).

Thus Na_vs are essential to trigger GABA release from the reciprocal spines.

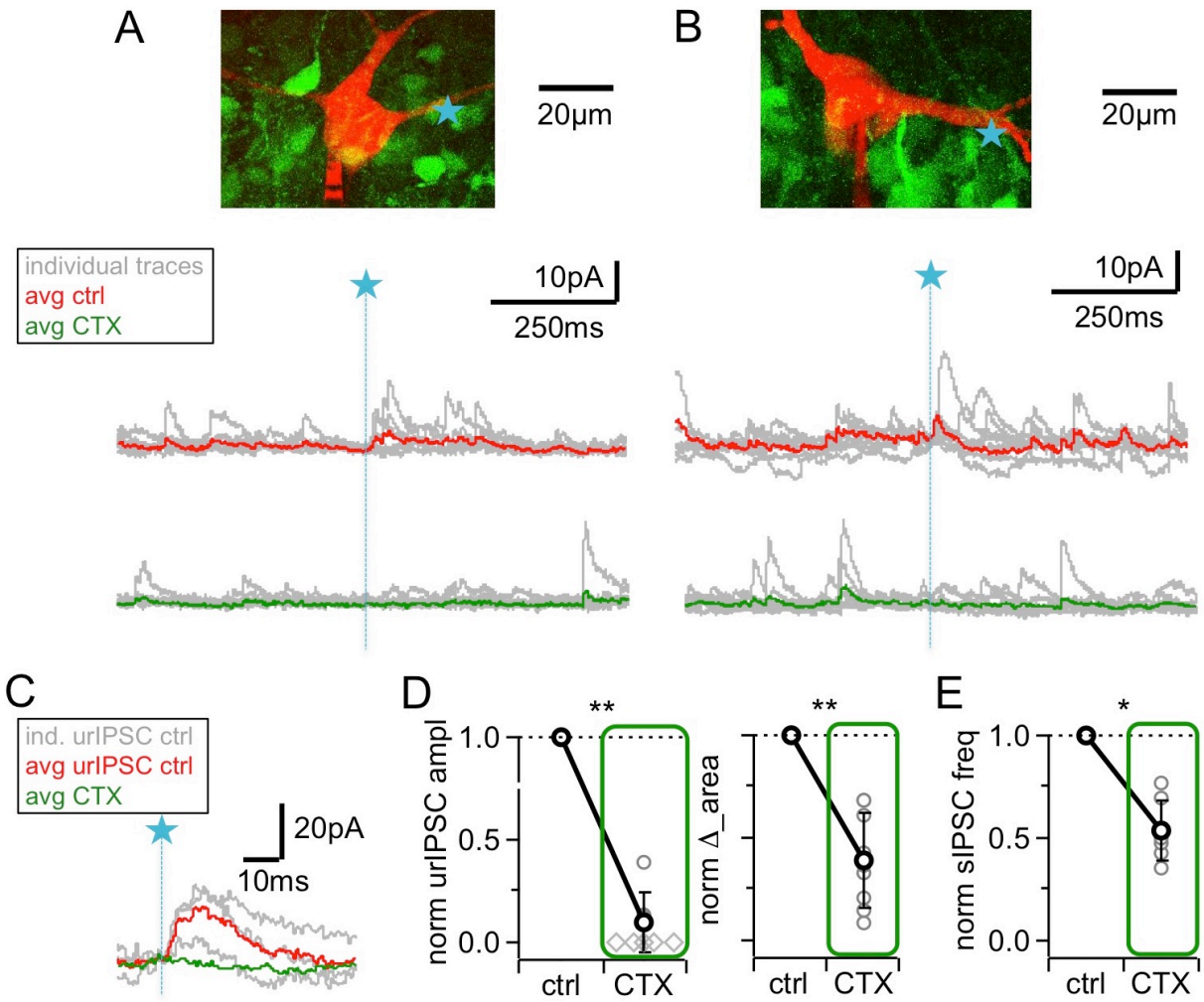

Figure 3. Blockade of high voltage activated Ca^{2+}-channels by ω-conotoxin MVIIC (CTX, 1 µM) causes a prominent reduction of urIPSC amplitudes.
(**A, B**) Two representative experiments in brain slices from VGAT-Venus rat with the corresponding MC (red), the site of TPU (blue star) and the uncaging traces according to the condition (individual traces : grey, average control: red, average CTX: green).
(**C**) Left: Magnified illustration of traces in B (for control individual traces with urIPSC responses and their average, for CTX only average, color coding as above).
(**D**) Left: Summary of effects of CTX on average normalized urIPSC amplitude (n = 8). Diamonds indicate the experiments with no detectable response in the presence of the drug. Right: Comparison of delta urIPSC areas normalized to control versus in the presence of CTX (n = 9).
(**E**) Inhibitory effect of CTX on spontaneous IPSC frequency (n = 7). See also A,B.

High-voltage activated Ca^{2+} channels in the spine trigger GABA release

HVACCs have been implied to mediate recurrent release from reciprocal spines (*Isaacson 2001*) and are activated by Na_vs, contributing a substantial fraction to the total postsynaptic Ca^{2+} signal in the GC spine (*Bywalez et al. 2015*). To directly test whether HVACC activation is required for release of GABA, we blocked NPQ-type Ca^{2+} channels with 1 µM ω-conotoxin MVIIC (CTX; *Bloodgood & Sabatini 2007; Bywalez et al. 2015*).

234 Fig. 3 shows the resulting substantial decrease of urIPSCs, to a fraction of 0.08 ± 0.14 of
235 control (from a mean amplitude of 11.3 ± 5.7 pA; n = 8, P < 0.005, Fig. 3D). This decrease
236 was not different from the effect of TTX on urIPSC amplitude described above (P = 0.35,
237 ratios in CTX vs TTX). Δ_area decreased to 0.39 ± 0.23 of control (n = 9, P < 0.005, Fig. 3D),
238 again statistically not different from the effect of TTX on Δ_area described above (P = 0.15 vs
239 TTX).
240 CTX decreased sIPSC frequency to a fraction of 0.53 ± 0.15 of control, less markedly than
241 TTX (Fig. 3E, n = 7 cells, control vs CTX: P < 0.01; CTX vs TTX: P < 0.005).
242 We conclude that HVACC activation is required for release of GABA from the reciprocal
243 spine following local input.
244 *NMDA receptors are also relevant for recurrent release*
245 NMDARs are known to substantially contribute to unitary synaptic transmission and to
246 postsynaptic Ca^{2+} entry at the MC to GC synapse (*Isaacson & Strowbridge 1998; Schoppa et*
247 *al. 1998; Isaacson 2001; Egger et al. 2005*). However, because NMDAR-mediated Ca^{2+} entry
248 into GC spines did not depend on Na_v activation in our previous study (in contrast to HVACC-
249 mediated Ca^{2+} entry, *Bywalez et al. 2015*), and because of the strong blocking effects of TTX
250 or CTX on urIPSCs reported above, we hypothesized that NMDAR blockade would have only
251 mild effects on fast recurrent release upon single inputs. Intriguingly however, Fig. 4 shows
252 that the application of 25 μM D-APV resulted in a substantial decrease of urIPSC amplitudes,
253 to on average 0.22 ± 0.21 of control (from a mean amplitude of 13.8 ± 8.6 pA, n = 10, P <
254 0.002, Fig. 4D). All individual experiments showed the amplitude decrease, albeit to a
255 variable degree (range 0.00 - 0.68 of control). Δ_area following TPU decreased to 0.40 ±
256 0.28 of control (n = 10, P < 0.003, Fig. 4D). Both effects were statistically not different from
257 the effects of either TTX or CTX (amplitude: P = 0.12 and P = 0.08; Δ_area: P = 0.19 and P =
258 0.47).
259

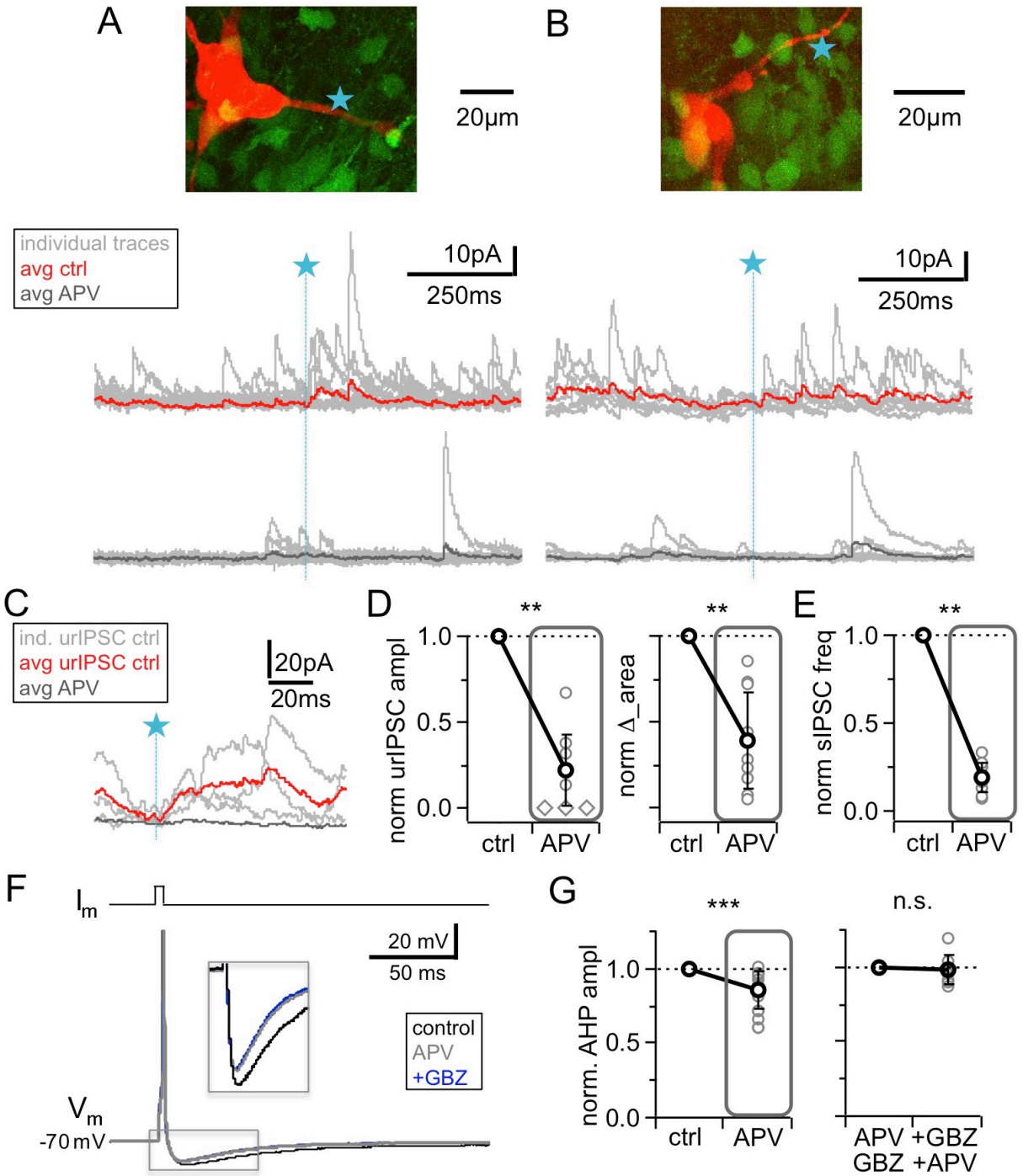

Figure 4. NMDAR blockade with D-APV (25 µM) results in a strong reduction of urIPSC amplitudes and also reduces AHPs following mitral cell APs

(**A, B**) Two representative uncaging experiments with the corresponding MC (red), the site of TPU (blue star) and the uncaging traces according to the condition (individual traces: grey, average control: red, average APV: dark grey); both VGAT-Venus.

(**C**) Magnified illustration of traces in A (for control individual traces with urIPSC responses (grey) and their average (red), for APV only average (dark grey)).

(**D**) Left: Summary of effects of APV on average normalized urIPSC amplitude (n = 10). Diamonds indicate the experiments with no detectable response in the presence of the drug. Right: Comparison of delta urIPSC integrals between control versus in the presence of APV (n = 10).

(**E**) Cumulative effect of APV on spontaneous IPSC frequency; see also A,B (n = 9).

(**F**) Representative example of MC AP evoked by somatic current injection in control conditions (black trace) and in the presence of APV (grey trace) and added GBZ (20 µM; blue trace). Inset: Magnified AHPs.

(**G**) Left: Cumulative effects of APV on average normalized AHP amplitude (n = 11 MCs). Right: Effect of occlusion experiments on AHP amplitude (APV before GBZ or GBZ before APV, n = 8).

278 APV also substantially reduced sIPSC frequency, to 0.19 ± 0.08 of control (n = 9, P < 0.01,
279 Fig. 4E), similar to TTX (P = 0.84) and significantly more pronounced than CTX (P < 0.001).
280 Since the strength of the effect of NMDAR blockade on urIPSCs was surprising to us, we
281 sought to provide another line of evidence for these findings in an experimental setting that
282 does not involve uncaging of glutamate (which might preferentially activate NMDARs, see
283 Discussion). The afterhyperpolarization (AHP) following single MC APs elicited by somatic
284 current injection was found to mainly reflect recurrent inhibition in brain slices from adult
285 mouse (*Nunes & Kuner 2018*), while in juvenile rat inhibitory synaptic contributions to the
286 AHP were observed to be less substantial but still detectable (on the order of 20-30% relative
287 to the K^+ channel-mediated component, *Dumenieu et al. 2015*). We used this paradigm to
288 test whether NMDAR blockade alone could interfere with recurrent inhibition (Fig. 4F, G).
289 Single MC AP AHPs (n = 13 MCs, V_{hold} = -70 mV) had a mean amplitude ΔV_m = – 9.5 ± 2.1
290 mV and a mean half duration $t_{1/2}$ = 43 ± 25 ms. Fig. 4G shows that APV application
291 significantly reduced the mean AHP amplitude to a fraction of 0.86 ± 0.12 of control (P <
292 0.001, Wilcoxon test; reduction in 12 of 13 MCs), while the half duration was not changed
293 (fraction of control 1.02 ± 0.42, P = 0.65). Next, to block $GABA_A$Rs we turned to gabazine
294 (GBZ, 20 µM), since Bicuculline might affect the K^+ channels that contribute to slow AHPs
295 (*Khawaled et al. 1999, Dumenieu et al. 2015*). GBZ alone caused a slightly stronger
296 reduction than APV, which was not significantly different (to 0.71 ± 0.10 of control, n = 7
297 MCs, P = 0.08 vs APV, not shown). Occlusion experiments using APV before GBZ or GBZ
298 before APV did not result in any further reduction (0.98 ± 0.10 of amplitude in presence of
299 first drug, n = 8 MCs, P = 0.45, Fig. 4F,G). Thus these experiments also support a
300 substantial role of GC NMDARs for GABA release.
301 From these and the uncaging experiments we conclude that NMDARs located on GCs are
302 strongly involved in reciprocal release, even though prevention of HVACC activation (via Na_v
303 block or pharmacology) also blocks reciprocal release. What is the underlying mechanism?
304 The simplest explanation for a cooperation would be a summation of NMDAR- and HVACC-
305 mediated Ca^{2+} currents at the presynaptic Ca^{2+} sensor. For this scenario two requirements
306 need to be satisfied: (1) temporal overlap of Ca^{2+} currents and (2) spatial proximity of
307 NMDARs and HVACCs within the same microdomain.

308 *Temporal overlap: Simulations of GC spine Ca^{2+} currents via HVACCs and NMDARs*

309 In conventional glutamatergic synapses the NMDAR-mediated postsynaptic current is rising
310 rather slowly compared to the AMPAR-mediated component (rise time ~ 10 ms, *Lester et al.*
311 *1990*) and therefore the fractional NMDAR Ca^{2+} current seems at first an unlikely candidate
312 to make direct contributions to fast release. In the reciprocal GC spines however, Na_v
313 channels are locally activated, which enables fast and substantial NMDAR activation. Fig. 5A
314 shows a simulation of the postsynaptic NMDAR- and HVACC-mediated Ca^{2+} currents (based
315 on the detailed NEURON model described in *Aghvami et al. 2019*, see Methods) which
316 illustrates that the local AP causes a transient boosting of the NMDAR Ca^{2+} current because
317 of further relief of the Mg^{2+} block during the upstroke and overshoot of the spine spike.
318 According to the simulation this fast NMDAR-mediated Ca^{2+} spikelet begins even before the
319 HVACC-mediated current and tightly overlaps with it within > 1 ms. Thus HVACC- and
320 NMDAR-mediated Ca^{2+} currents could act in a cooperative manner at the Ca^{2+} sensor(s) that
321 mediate fast release of GABA, especially so, if the release probability was proportional to the
322 fourth power of local $\Delta[Ca^{2+}]$ or more as at other central synapses, and if the channels were
323 close enough to form a microdomain, allowing for an 'overlap bonus' (*Stanley 2016*; Fig. 5B).
324 In the temporal domain, this overlap was found to be highly robust against the variation of the
325 combined Na_v/K_v conductance, and increases in either AMPAR conductance g_{AMPA} or neck
326 resistance R_{neck} resulted in an earlier activation of both HVACC and NMDAR-mediated Ca^{2+}
327 currents and even stronger overlap (Fig. 5C, see Methods). Decreases resulted at first in
328 little change and then a loss of the spine spike whereupon there is no more HVACC
329 activation. To illustrate specifically the contribution of the Na_v-mediated boosting of the
330 NMDAR-mediated Ca^{2+} current, we also calculated the overlap bonus for the HVACC-
331 mediated current as above and the NMDAR current in absence of the spine spike, which
332 indeed renders the cooperative effect negligible (Fig. 5B).

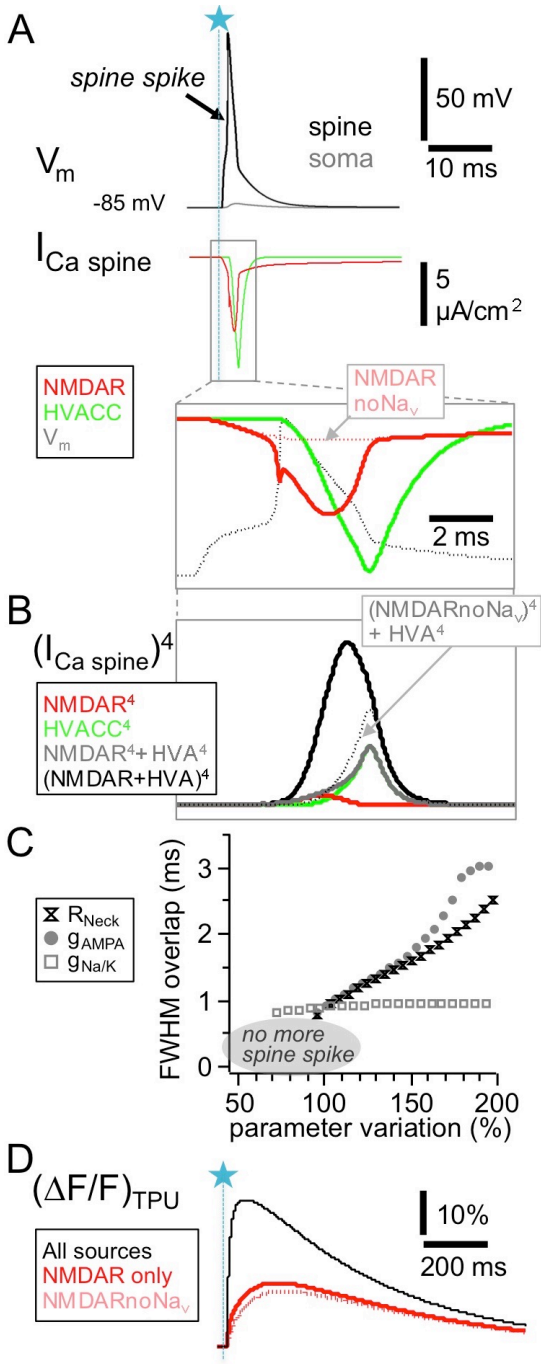

Figure 5. HVACC- and NMDAR-mediated Ca^{2+}-currents overlap temporally in the wake of the spine spike. Simulated spine Ca^{2+}-currents and $(\Delta F/F)_{TPU}$

(**A**) Top panels: spine membrane potential V_m and Ca^{2+}-currents (as in *Aghvami et al. 2019*, their Fig 2B, but without exogenous Ca^{2+} buffer). Bottom: Blow-up of NMDAR- and HVACC-mediated Ca^{2+}-currents, overlaid with the membrane potential V_m. Note the early onset of the NMDAR Ca^{2+}-current and its increase during the underlying local action potential. Red dotted line: NMDAR Ca^{2+}-current in the absence of Na_vs.

(**B**) The temporal coincidence creates an ‚overlap bonus' with respect to local Ca^{2+} concentration and triggering of release: Fourth power of single and added Ca^{2+}-currents. Black dotted line: Addition (hypothetical!) of HVACC with NMDAR Ca^{2+}-current in the absence of Na_vs.

(**C**) Robustness test for extent of overlap between NMDAR- and HVACC-mediated Ca^{2+}-current. Overlap is measured as the stretch of overlapping FWHMs of the current transients (Full Width Half Maxima, see Methods). Parameter variation within 50 - 200% of the nominal value of the neck resistance R_{neck}, the AMPAR conductance gAMPA and the coupled Na_v/K_v conductance $g_{Na/K}$. Results are shown only for parameter runs with spine spike.

(**D**) Simulated fluorescence transients ΔF/F (in the presence of 100 µM OGB-1) show that the contribution of the Na_v-mediated boost of NMDAR Ca^{2+}-currents to the total NMDAR-mediated Ca^{2+} signal is almost negligible (see Discussion).

Spatial proximity: Ultrastructural evidence for presynaptic localization of NMDARs

For fast neurotransmitter release to occur, the current view is that Ca^{2+} entry needs to happen in a proximity of 100 nm or less from the Ca^{2+} sensing part of the SNARE machinery (reviewed in *Kaeser & Regehr 2014; Stanley 2016*). Therefore, to permit cooperation of Ca^{2+} influxes, NMDARs should be localized very close to or within the GABAergic presynapse. Earlier electron microscopic (EM) studies had reported the presence of postsynaptic NMDARs in GC spines and also instances of extrasynaptic labeling (*Sassoè-Pognetto & Ottersen 2000, Sassoè et al. 2003*). To test for the presence of NMDARs near or within GABAergic active zones, we analysed GC spine heads in ultrathin sections that were

immunogold-labeled with either GluN1 or GluN2A/B antibodies (Fig. 6A; see Methods); the sections were selected for the presence of at least one asymmetric (i.e. glutamatergic) contact and/or one symmetric (i.e. GABAergic) contact.

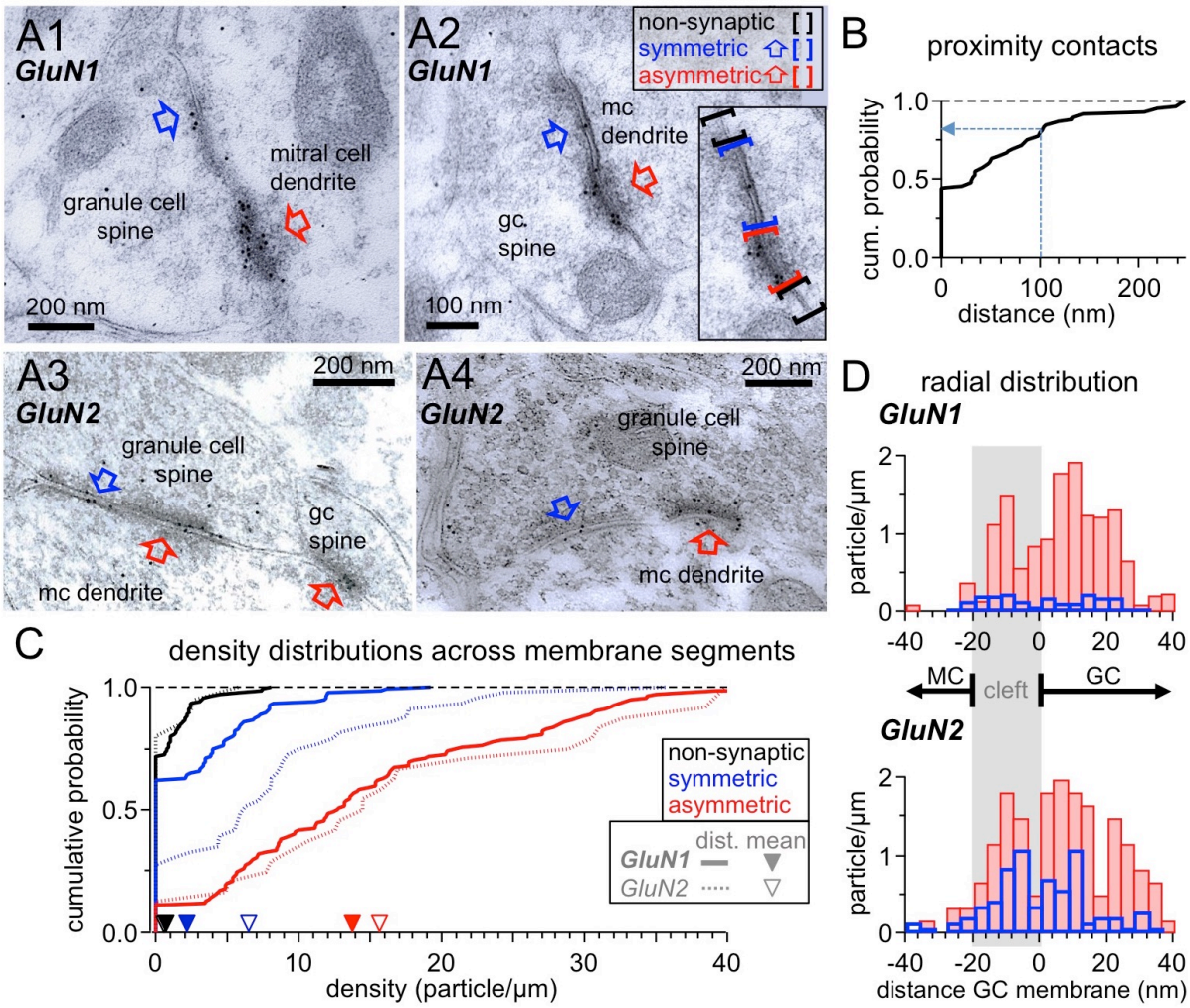

Figure 6. Ultrastructural analysis of the distribution of NMDARs shows their presence at both post- and presynaptic GC spine membranes in reciprocal dendro-dendritic synapses.
(**A**) Representative micrographs of reciprocal dendrodendritic synapses labeled for GluN1 (A1, A2) and GluN2A/B (A3, A4). Note that asymmetric MC-to-GC synapses (red arrows) are strongly labeled and that symmetric GC-to-MC junctions (blue arrows) are also immunopositive. Gold particles are usually not associated with non-synaptic plasma membrane domains of GC spines. The inset in panel A2 illustrates the selection of non-synaptic membrane segments (black brackets), symmetric synapses (blue) and asymmetric synapses (red).
(**B**) Frequency distribution of distances between symmetric and asymmetric synaptic profiles on the same GC spine membrane (based on n = 60 micrographs with both types of profiles on the same spine).
(**C**) Frequency distributions of labeling densities across synaptic (symmetric and asymmetric) and non-synaptic membrane segments for GluN1 (thick lines) and GluN2A/B (thin dotted lines). The arrows on the x-axis indicate the mean density (GluN1: solid, GluN2A/B: open). Color code as in (A).
(**D**) Radial distribution of gold particles representing GluN1 (top panel) and GluN2A/B (bottom panel) at asymmetric (red) and symmetric (blue) synapses. Particle numbers were normalized to the total length of the respective synaptic segments.

364 Interestingly, we observed that when both symmetric and asymmetric synaptic profiles were
365 visible in individual GC-MC dendrodendritic pairs, the two synaptic profiles were mostly either
366 contiguous (44% of n = 60 cases, examples Fig. 6A2,A3, cumulative plot Fig. 6B) or closer
367 than 100 nm (36% of cases). This finding implies that on both sides of the dendrodendritic
368 synaptic arrangement the postsynaptic specialization very often merges with presynaptic
369 release sites without interposition of non-synaptic membrane domains, and that therefore on
370 the GC side postsynaptic NMDARs can be located very closely to the GABAergic
371 presynapse.
372 Immunogold labeling for NMDARs was also frequently observed in symmetric contacts, albeit
373 at a lesser density compared to asymmetric contacts (Fig. 6A). To establish whether there is
374 an increased likelihood for the presence of NMDARs at symmetric contacts versus
375 extrasynaptic profiles, we compared the densities of labeling in non-synaptic membrane
376 segments of GC spines with those in symmetric synapses, and as a control in asymmetric
377 synapses. GC spines establishing synapses with MC dendrites were selected as described
378 (see Methods) and all discernible membrane segments within a spine were analysed. For
379 GluN1, there were 50 particles along 84.5 µm of 138 non-synaptic spine membrane
380 segments (mean 0.6 particles/µm), 70 particles along 32.7 µm of 120 symmetric profiles
381 (mean 2.1 particles/µm) and 394 particles along 28.6 µm of 111 asymmetric profiles (mean
382 13.8 particles/µm). Fig. 6C shows the density distributions across the three types of
383 membrane segments. The distribution of the density of gold particles at symmetric synapses
384 was significantly higher than the one in non-synaptic membrane (P = 0.000029, Kolmogorov-
385 Smirnov test). For GluN2A/B, the sample size was smaller, with 5 particles along 10.0 µm of
386 24 non-synaptic spine membrane segments (mean 0.5 particles/µm), 89 particles along 14.0
387 µm of 46 symmetric profiles (mean 6.4 particles/µm) and 96 particles along 6.1 µm of 25
388 asymmetric profiles (mean 15.7 particles/µm). Still, the density distribution at symmetric
389 synapses was significantly higher than the distribution at the non-synaptic membrane (P =
390 0.000048).
391 Interestingly, while the labeling densities for GluN1 and also GluN2A/B were similar across
392 non-synaptic membranes and asymmetric synapses (P = 0.99 and P = 0.81, respectively),
393 labeling of symmetric synapses was considerably stronger for GluN2A/B versus GluN1 (P =

394 0.00042). This difference might be due to a distinct receptor configuration and/or a better
395 accessibility of the GluN2 epitopes in the presynaptic symmetric membrane.
396 Finally, we analysed the radial distribution of particles across synaptic profiles for both
397 antibodies to establish whether labeling was predominantly associated with either the GC or
398 the MC membrane (Fig. 6D; see Methods). The distribution of both GluN1 and GluN2A/B
399 label at asymmetric synapses was similar, with a main peak just inside the postsynaptic GC
400 membrane and another peak within the synaptic cleft. Only a few gold particles were
401 localized beyond 20 nm on the MC side, suggesting that NMDARs are not expressed at
402 significant levels at the glutamate release sites on the MC membrane. Notably, the
403 distribution of gold particles at symmetric synapses mirrored the one at asymmetric
404 synapses, implying that labeling for NMDARs is predominantly associated with both the
405 presynaptic GABAergic and the postsynaptic glutamatergic membrane of GCs.
406 In summary, we conclude from these findings that NMDARs do play a direct presynaptic role
407 for GABA release from the reciprocal spine, albeit in cooperation with HVACCs (Fig.7). A
408 direct consequence of this conclusion is that any inhibitory output from a GC spine will
409 require the presence of glutamate and thus synaptic input to the respective spine, with far-
410 ranging implications for the role of GC-mediated lateral inhibition in early olfactory processing
411 (see Fig. 8, Fig. 9, Discussion).

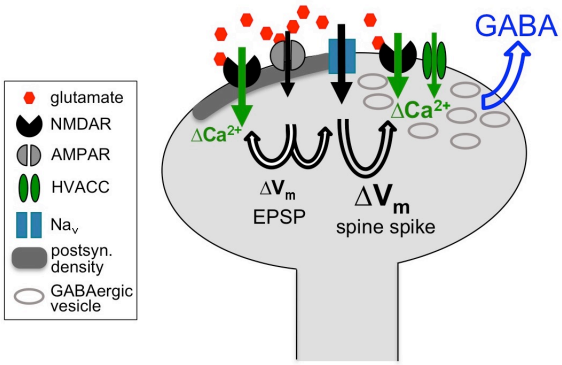

412
413

Figure 7 Cooperative release of GABA from the granule cell reciprocal spine
Depolarizing currents are indicated by black solid arrows and Ca^{2+} entry by green solid arrows. Upon binding of glutamate, AMPARs get activated, leading to depolarization of the spine, then activation of both post- and presynaptic NMDARs and Na_vs. The latter in turn drive further depolarization, i.e. the spine spike, which both activates HVACCs and enhances Ca^{2+} entry via NMDARs by additional relief of their Mg^{2+} block. HVACC- and presynaptic NMDAR-mediated Ca^{2+}-currents cooperate to promote release of GABA.

414 ***Discussion***

415 Here we have demonstrated that mimicking unitary synaptic inputs via two-photon uncaging
416 of glutamate onto individual olfactory bulb GC spines can activate the entire microcircuit
417 within the spine, from the local spine spike to the release of GABA onto MC lateral dendrites,
418 proving the mini-neuron-like functionality of the reciprocal microcircuit. As in classical axonal
419 release, sequential Na_v channel and HVACC activation triggers output, which occurs on both
420 fast and slow time scales. Strikingly, however, presynaptic NMDA receptors are also found to
421 play a role for GABA release. These findings together with other prior knowledge allow to
422 make an educated guess regarding the specific function of reciprocal spines in bulbar
423 processing (see further below).

424 *Properties of microcircuit operation and implications for coincident local and global activation*

425 For the proximal reciprocal GC inputs investigated here we estimate that under physiological
426 conditions close to the MC resting potential the size of the fast IPSCs is on the order of -5
427 pA, after corrections for the partial $GABA_AR$ block by DNI and the setting of E_{Cl}. Thus,
428 assuming an *in vivo* MC input resistance of 100 MΩ (*Angelo & Margrie 2011*), an inhibitory
429 input from a single GC spine will exert a somatic hyperpolarization of at best 0.5 mV, and
430 therefore even proximal GC inputs will barely influence MC firing (*Fukunaga et al. 2014;*
431 *McIntyre & Cleland 2016*) - unless there is coordinated activity across GC spines connected
432 to the same MC dendrite, for example in the wake of an MC action potential during the
433 recurrent IPSP (see e.g. Fig. 4F) or during gamma oscillations (e.g. *Kay 2003; Lagier et al.*
434 *2004*).

435 Upon local activation we observed a GABA release probability P_{r_GABA} from the GC spine on
436 the order of 0.33. This value might represent an upper limit, because the global reduction of
437 inhibition by DNI could cause a homeostatic upregulation of P_{r_GABA} (e.g. *Rannals & Kapur*
438 *2011*), and the detection of connections is generally biased towards larger P_{r_GABA}.

439 With $P_{r_GABA} \approx 0.3$ and the probability for MC glutamate release on the order of $P_{r_Glu} \approx 0.5$ –
440 0.75 (*Egger et al. 2005; Pressler & Strowbridge 2017*) the efficiency of the entire reciprocal
441 microcircuit can be estimated as $P_{reciprocal} = P_{r_Glu} \cdot P_{r_GABA} \approx 0.2$, possibly informing future
442 network models. The rather low P_{r_GABA} observed here also implies that GC spines are likely
443 to release with higher probabilities upon coincident global GC signalling (Ca^{2+} spike or global

444 action potential), due to substantially increased ΔCa^{2+} in the spine (*Egger et al. 2005; Egger*
445 *2008; Aghvami et al. 2019; Mueller & Egger 2020)*. We predict this effect to boost both
446 recurrent and lateral inhibition, as described below (Fig. 9).
447 As to the minimal latency for recurrent GABA release, the temporal resolution of our
448 experiments is limited by the uncaging laser pulse duration (1 ms) and by the unknown exact
449 time course $V_m(t)_{SPINE}$ of the spine spike. Fig. 1E shows that the fastest urIPSCs were
450 detected within 2 ms from TPU onset, implying that there is a fast mechanism coupling Ca^{2+}
451 entry to release - in line with earlier findings of tight coupling between Ca^{2+} entry and GABA
452 release (using EGTA, *Isaacson, 2001*), and of a crucial role for Na_v channels (*Bywalez et al.*
453 *2015; Nunes & Kuner 2018*).
454 While ~ 30% of urIPSCs occurred within 10 ms post TPU onset, there was also a substantial
455 fraction with longer latencies in the range of 10 - 30 ms and some even larger delays. Again,
456 since $V_m(t)_{SPINE}$ is unknown, we cannot determine to what extent these urIPSCs were actually
457 asynchronous (if defined as release events that happen later than the fast coupling of HVA
458 presynaptic Ca^{2+} currents to the release machinery, e.g. *Kaeser & Regehr 2013).* In any
459 case, substantial asynchronous release from the GC spine on yet longer time scales
460 (detected at up to 500 ms post TPU) was frequently observed, in line with earlier studies on
461 recurrent inhibition that localized the origin of asynchronous signalling within GCs (*Schoppa*
462 *et al. 1998; Chen et al. 2000; Isaacson 2001)*. This time course of asynchronous release also
463 matches with the duration of physiological postsynaptic GC spine Ca^{2+} transients (*Vanessa*
464 *Lage-Rupprecht & Veronica Egger, unpublished observation*). Thus, the microcircuit can
465 operate across a wide range of latencies, which might contribute to glomerulus-specific GC
466 global AP firing latencies (*Kapoor & Urban 2006*), and also can generate combined
467 synchronous and asynchronous output.
468 *Na_v-mediated and NMDAR-mediated contributions to release*
469 How is postsynaptic Ca^{2+} entry coupled to release of GABA within the GC spine? Previously
470 we have shown via occlusion experiments that Ca^{2+} entry via NMDARs occurs independently
471 from Ca^{2+} entry mediated by the Na_v-HVACC pathway, since AMPAR-mediated
472 depolarization on its own is strong enough to lift the Mg^{2+} block, probably due to boosting by
473 the high GC spine neck resistance *(Bywalez et al. 2015)*. Therefore, we initially hypothesized

474 that the Na_v-HVACC pathway would provide the sole trigger for fast release of GABA, as in
475 classical release from axons (see also *Nunes & Kuner 2018*), reinforcing the notion of the
476 GC spine as an independent mini-neuron that can generate output via its own local AP.
477 Indeed, blockade of either Na_v or HVACCs strongly reduced or abolished urIPSCs. However,
478 in subsequent experiments probing NMDAR contribution we observed that urIPSCs were
479 also massively reduced by blockade of NMDARs.
480 As a note of caution, activation of single GC spines via TPU might involve spurious activation
481 of extrasynaptic NMDARs. We had observed that TPU resulted in a slightly larger NMDA-
482 receptor mediated component of the postsynaptic Ca^{2+} signal than true synaptic activation
483 via glomerular stimulation (~ 65 % vs ~ 50% of ΔF/F, *Bywalez et al. 2015; Egger et al. 2005*).
484 Thus, at least part of the strong impact of NMDARs observed here might have been rooted in
485 their over-activation. Therefore, we investigated recurrent inhibition elicited by single MC
486 APs, and could demonstrate that NMDAR blockade alone (which does not prevent GC spine
487 spike generation, *Bywalez et al. 2015*) also reduces recurrent inhibition. This effect was
488 found to be mutually occlusive with the effect of $GABA_AR$ blockade, arguing again in favor of
489 an essential role of NMDARs for GABA release and against systematic overstimulation in the
490 TPU experiments (see also Results, Methods).
491 Another interesting aspect of the strong influence of NMDARs on GC output is that this
492 property might serve to differentiate the MC↔GC microcircuit from the MC↔PV+ cell
493 microcircuit, since PV+ cells feature Ca^{2+}-permeable AMPARs and a probably absent
494 NMDAR component in response to MTC input (*Kato et al. 2013*). Thus, the urIPSC blockade
495 by APV observed here further argues in favor of a preferential activation of the MC↔GC
496 circuit by our experimental method.
497 In our previous study of postsynaptic Ca^{2+} signals in GC spines there was no obvious
498 influence of Na_v activation on NMDAR-mediated Ca^{2+} entry (*Bywalez et al. 2015*). At first, this
499 finding might seem at variance with the simulations in Fig. 5 that demonstrate a boosting of
500 early NMDAR-mediated Ca^{2+} currents by the spine spike. However, the simulations also
501 indicate that this extra contribution is not substantial in terms of added ΔF/F under our
502 experimental conditions and therefore could not be detected (Fig. 5D). In line with the fast
503 NMDAR-mediated Ca^{2+} spikelet, *Kampa et al. (2004*) have shown that the earlier the

504 postsynaptic membrane is depolarized after glutamate release, the more efficiently NMDARs
505 will be activated. These observations are of general importance in the context of spike-timing
506 dependent plasticity and electrical compartmentalization of spines (e.g. *Grunditz & Oertner*
507 *2004, Tonnesen & Nägerl 2016*).
508 How exactly do NMDARs now effect release? The Na_v/NMDAR-mediated Ca^{2+} spikelet
509 results in substantial and fast coincident activation of NMDARs and HVACCs, and our
510 ultrastructural evidence for presynaptic NMDARs implies that indeed these currents can feed
511 into the same presynaptic microdomain (see Results). This overlap bonus at the presynaptic
512 Ca^{2+} sensor (as predicted by the simulations) is likely to underlie the observed cooperative
513 signalling of HVACCs and NMDARs.
514 *Direct involvement of presynaptic NMDARs in GABA release*
515 Presynaptic actions of NMDARs at specific subsets of both glutamatergic and GABAergic
516 synapses have recently received attention (reviewed *in Bouvier et al. 2015; Banerjee &*
517 *Paulsen 2016*). Presynaptic NMDARs have been shown to play a role in plasticity induction
518 (e.g. *Duguid & Smart 2004*) or in modulation of basal synaptic transmission, where effects
519 are mostly observed upon repetitive transmitter release (e.g. *McGuiness et al. 2010*).
520 Presynaptic NMDARs in the cerebellum are also involved in enhancing spontaneous release
521 of GABA (*Glitsch & Marty 1999*), with similar recent observations for extrasynaptic NMDA
522 receptors on retinal A17 amacrine cells (V*eruki et al. 2019*). However, to our knowledge
523 direct triggering of release via presynaptic NMDARs during unitary transmission has not
524 been observed so far, adding another pathway to the already highly diverse signalling
525 downstream of NMDARs.
526 The observed cooperation between Na_v/HVACCs and NMDARs relates our study back to the
527 initial studies on dendrodendritic recurrent inhibition (DDI), when it was concluded by several
528 groups that NMDARs can contribute directly to release from the reciprocal spine upon
529 extended release of glutamate from the MC dendrite (see Introduction), and *Schoppa et al.*
530 *(1998*) already speculated that this presynaptic function might be related to either Ca^{2+} entry
531 or depolarization. However, the relative contribution of NMDARs has been under debate and
532 it was demonstrated that under physiological conditions HVACC activation would be the
533 dominant release trigger (*Isaacson 2001*). While the standard DDI protocol, using 20-50 ms

534 long depolarizations, would evoke recurrent inhibition also in the presence of TTX (possibly
535 even enhanced, *Halabisky et al. 2000*), it was reported that recurrent inhibition in response to
536 shorter steps (< 5 ms) is substantially smaller than for the long step and reduced in TTX
537 (*Schoppa et al. 1998; Halabisky et al. 2000*). In view of our above findings, the standard DDI
538 protocol is likely to recruit NMDAR-dependent pathways for triggering GABA release via
539 prolonged release of glutamate and subsequent summation of EPSPs in GC spines,
540 whereas short steps are more likely to trigger release via the GC spine spike. Thus, the
541 cooperation of NMDARs and HVACCs reconciles these earlier findings.

542 *Reciprocal inhibition and spontaneous inhibitory activity*

543 Spontaneous IPSCs are likely to predominantly originate from the more proximal lateral MC
544 dendrites (*Arnson & Strowbridge 2017*). The slightly larger mean amplitude of sIPSCs
545 compared to the triggered urIPSCs observed here might be explained by perisomatic
546 inhibitory contacts onto MCs, e.g. from type S GCs (*Naritsuka et al. 2009*). All three
547 antagonists of urIPSC generation (TTX, CTX, APV) were found to also substantially reduce
548 sIPSC frequency. For Na_v blockade, strong effects on MC sIPSCs were reported also
549 elsewhere (e.g. *Halabisky et al. 2000; Arnson & Strowbridge 2017*) and are expected
550 because of the blockade of spontaneous MC firing and the GC spine spike. The effect of
551 HVACC blockade was less pronounced than that of Na_vs, probably because it will not
552 prevent spontaneous MC firing.

553 The substantial effect of NMDAR blockade on spontaneous IPSCs was also observed in
554 other olfactory bulb studies (*Wellis & Kauer 1993; Schmidt & Strowbridge 2014; but see*
555 *Chen et al. 2000*). Several factors might contribute: (1) the long-lasting depolarizations in
556 MCs that are enhanced by NMDAR activation (*Carlson et al. 2000*), (2) the presence of MC
557 NMDA autoreceptors (*Sassoé-Pognetto et al. 2003*), and (3) the crucial role of NMDARs for
558 release from the GC spine reported here, since spontaneous release of glutamate from MCs
559 is unlikely to trigger recurrent IPSCs in the presence of APV.

560 *Functional role of presynaptic NMDARs in GC spines: Linking coactive glomerular columns*

561 While a presynaptic contribution of NMDARs to GABA release from GCs was already
562 demonstrated earlier (see above), our findings imply that not only **can NMDAR activation**

trigger GABA release, it is actually necessary, also in the presence of a Na_v-mediated spine spike. This observation is very intriguing for several reasons:

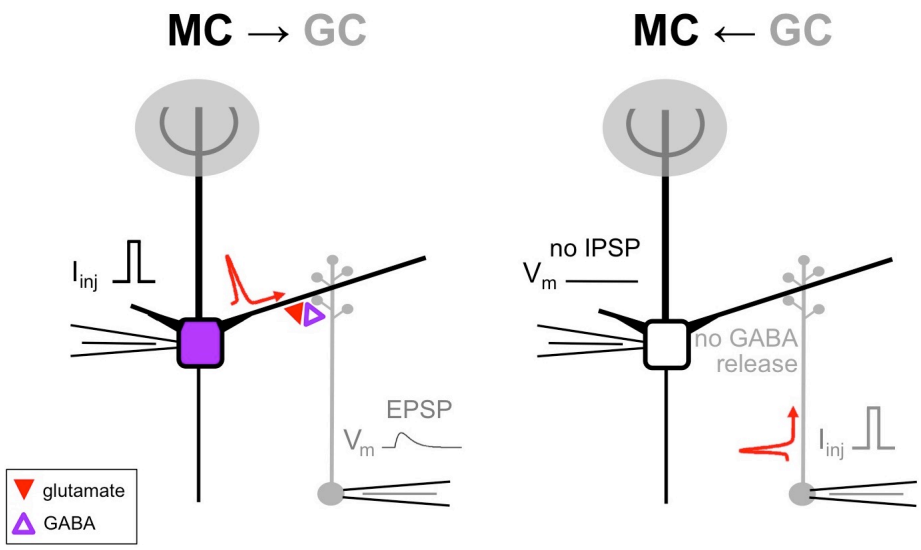

Figure 8. Action potentials alone are unlikely to cause release from GCs, thus no apparent reciprocal connectivity is oberved in coupled GC↔MC pairs.
Left: Recording situation for connection MC→GC. A MC action potential is elicited by somatic current injection and propagates along the lateral dendrite. An EPSP will be detected at the GC soma. Recurrent release of GABA will be triggered at the reciprocal synapse (see also Fig. 7).
Right: Recording situation for connection GC→MC. A GC action potential is elicited by somatic current injection and propagates into the apical dendrite and its spines. However, this action potential will not trigger release of GABA, since there is no glutamate present at the reciprocal synapse to activate the presynaptic NMDARs, and hence no IPSP will be recorded at the MC soma.

(1) No AP-mediated release from the reciprocal spine without synaptic input.

Notwithstanding the precise site of AP generation in GCs, any AP will propagate along the GC dendrite and the reciprocal spines perfectly well (*Egger et al. 2003, Pressler & Strowbridge 2019*). The ensuing spine depolarization $V_m(t)_{SPINE}$ will resemble that of the spine spike (*see also Aghvami et al. 2019*) which on its own, with NMDARs blocked, according to our findings cannot trigger GABA release. Therefore, any action potential that propagates within the GC is rather unlikely to cause release of GABA by itself. This consequence explains why no reciprocal connectivity was reported from paired recordings of MCs coupled to GCs so far (*Isaacson 2001, Kato et al 2013, Pressler & Strowbridge 2017*) and why others including our group have been unable to find connected GC → MC pairs in paired recordings in the first place (see *Egger et al. 2003, Schoppa 2006*), since functional connectivity is tested by eliciting APs in the putative presynaptic cell (see Fig. 8). This lacking proof of functional connectivity has been

590 particularly enigmatic in view of plenty of ultrastructural evidence that spines between
591 MCs and GCs are usually reciprocal (e.g. *Price & Powell 1970, Jackowski et al. 1978,*
592 *Woolf et al. 1991*), and of the strong physiological evidence for GC-mediated recurrent
593 inhibition of MCs. It should be noted that extracellular stimulation of the GC layer can
594 elicit MC inhibition, even in the presence of APV (*e.g. Chen et al 2000, Egger et al. 2003,*
595 *Arevian et al. 2008*). Possible explanations might be that either there is still some small
596 remaining probability for GABA release from spiking GCs in the absence of glutamate, or
597 that this type of stimulation activates some as of yet unknown inhibitory input to MCs, e.g.
598 via deep short-axon cells or axons of EPL interneurons (*Nagayama et al. 2014, Burton*
599 *2017*).
600 (2) Role of GC-mediated lateral inhibition between MCs.
601 It is known by now that broad, far-range lateral inhibition between mitral cells within the
602 EPL is mediated by other interneurons than GCs (see Introduction). Thus, GCs are
603 unlikely to dominate bulbar lateral inhibition in terms of magnitude, i.e. total charge
604 transfer, a view that is also supported by other recent studies (*Fukunaga et al. 2014,*
605 *Geramita & Urban 2017*). What then is the function of GC-mediated lateral inhibition?
606 Activation of a given olfactory receptor will in turn activate its associated glomerular unit
607 and the neurons belonging to the respective glomerular column. In the following, a given
608 GC belongs a glomerular column if it can be fired (globally or regionally) via the activation
609 of the MTCs associated with that column. Evidence for GC spiking upon uniglomerular
610 activation *in vitro* has been observed by several groups, including our own (e.g. *Schoppa*
611 *et al. 1998, Egger 2008, Stroh et al. 2012; Burton & Urban 2015*); moreover, we have
612 shown recently that rather low numbers of coactivated spines on GC apical dendrites (<
613 10) are sufficient to elicit dendritic spiking (*Mueller & Egger, 2020*).

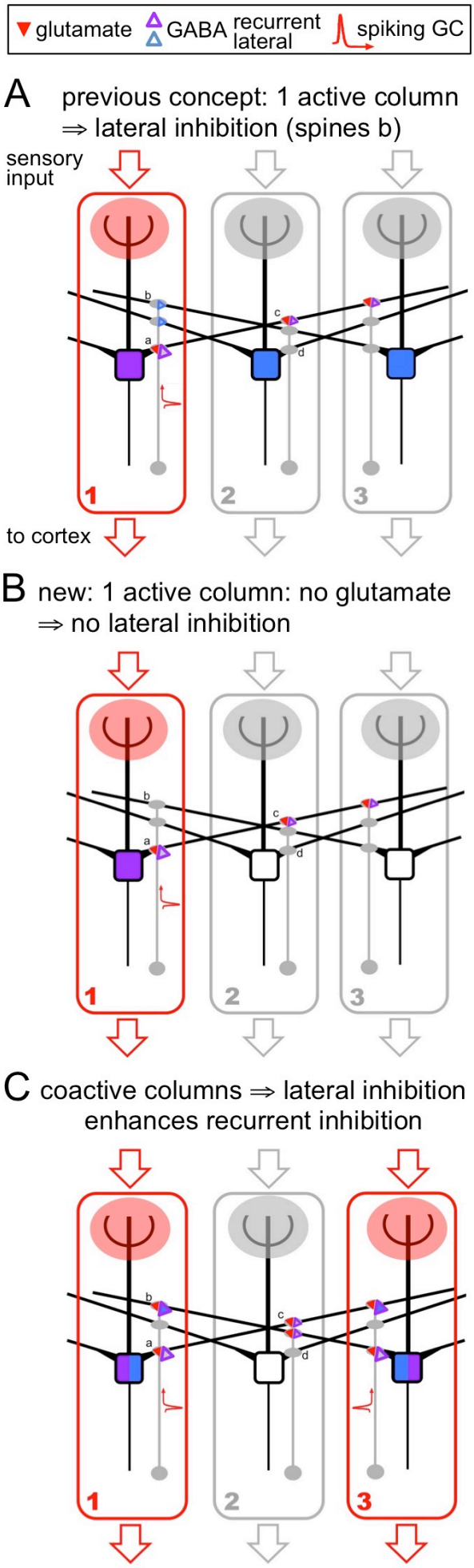

Figure 9 GC-mediated lateral inhibition: previous and new concept

In each schematic column, the depicted mitral cell and granule cell stand for the ensemble of all MCs and GCs belonging to the column. GCs belong to a column if they can be fired (globally or regionally) by the ensemble of active columnar MCs (and thus a given GC may belong to more than one column). All three columns are interconnected via MC-GC-MC interactions. There are four GC spine types: a: spines receiving MC input within the column, b: other spines that belong to GCs within the column but without columnar input, c: spines in other columns that are laterally connected to the active column, d: spines in other columns that are not laterally connected to the active column.

A Classical hypothesis

Column 1 gets activated by sensory input. Its MCs fire and receive recurrent inhibition from the GC spines they are connected to, both from within the column (spines a) and from others (e.g. spines c). Upon firing of the columnar GCs, these release GABA from their reciprocal spines, including contacts to other columns (spines b). Note that the columnar outputs (spines a) will exert stronger recurrent inhibition than the non-columnar spines c because of the coincidence of the GC spike with the local input. Thus recurrent inhibition at spines a will be enhanced. The MCs in column 1 will receive recurrent inhibition and the MCs in the other columns 2,3 will receive lateral inhbition.

B New hypothesis, scenario I: One active column.

If only one column is activated, lateral inhibition will not happen since spines b do not receive any glutamate and the propagating spike alone is not sufficient for GABA release (see also Fig. 8). Still, there will be recurrent inhibition from spines c. Note that the enhanced recurrent inhibition at spine a will also happen in this scenario.

C New hypothesis, scenario II: Coactive columns.

If two or more columns are coactive, again there will be enhanced recurrent inhibition at their spines a. In addition, spines b in column 1 will now exert recurrent inhibition of the coactive column 3 and this recurrent inhibition will be enhanced by the coincidence of the GC spike in column 1 with the lateral input, thus lateral inhibition will also be exerted. If the connectivity and the strength of activation are symmetric, the situation in column 3 is symmetric, resulting in mutual lateral inhibition and thus possibly synchronized output.

Thus the MCs within the active columns 1, 3 will receive recurrent inhibition enhanced by lateral inhibition and the MCs in the silent column 2 will not be inhibited at all. Even if the GCs in column 2 would become fired by multiple coincident lateral inputs, they will not release GABA on the MCs of column 2, since again there is no glutamate at the respective contacts.

614

615 Figure 9A illustrates the prevailing concept of GC-mediated lateral inhibition up to now.
616 Upon spiking (global or regional) the spikes will result in GABA release not only at the
617 reciprocal synapses that have received input from an active glomerulus but also in GABA
618 release from other spines invaded by the spike that connect to extra-glomerular mitral
619 cells, exerting lateral inhibition. The spatial structure of this lateral inhibition depends on
620 anatomical connectivity and network dynamics and has been proposed to be either
621 isotropic, consistent with a center-surround field as in the retina, or rather patchy
622 (reviewed in *Murthy 2011*; see also *Chae et al. 2019*). Note however, that most of the
623 involved studies did not investigate specifically GC-mediated lateral inhibition.
624 In any case, the columnar GC spines (i.e. those that receive synaptic input from the
625 active column) will experience coincident local spine spikes and global spikes, resulting
626 in enhanced local Ca^{2+} entry, and therewith are likely to increase their release probability
627 P_{r_GABA} (see above).
628 However, as a consequence of the requirement of presynaptic NMDAR activation, there
629 will be no or at best very little GC-mediated lateral inhibition upon activation of a single
630 column (Fig. 9B). We predict that GC-mediated **lateral inhibition will happen**
631 **predominantly across coactive columns**, such that a local synaptic input originating
632 from a lateral active column will coincide with a global (or regional) columnar spike,
633 resulting in enhanced inhibition of the lateral coactive column. The mechanism is the
634 same as for the coincidence detection described above for recurrent inhibition within an
635 active column (Fig. 9C). Provided that there are mutually interconnecting GCs in both
636 columns, this effect will be symmetric.
637 Therefore, GC-mediated lateral inhibition acts non-topographically (i.e. not isotropically)
638 to enhance recurrent inhibition. Non-topographical lateral interactions in the bulb have
639 been proposed already previously based on functional evidence and simulations (e.g.
640 *Urban & Arevian 2009, Shepherd et al. 2007, Fantana & Meister 2008*). While non-
641 topographic lateral inhibition may also happen within the glomerular layer (e.g. *Cleland &*
642 *Sethupathy 2006, Economo et al. 2016*), our hypothesis is built on the spine-specificity of
643 GABA release. It does not require a specific, pre-established anatomical connectivity but

644 is a property of the synaptic arrangement of the microcircuits. Connectivity is dynamically
645 restricted to coactive columns and thus matched to glomerular activation patterns.
646 This mechanism will allow GC-mediated lateral inhibition to participate in synthesizing the
647 olfactory percept at the level of the bulb from the individual olfactory receptor channels,
648 most likely via synchronization in the gamma band (e.g. *Laurent et al. 1996, Kashiwadani*
649 *et al. 1999, Schoppa 2006, Brea et al 2009, Li et al. 2015, Peace et al. 2017*), while at
650 the same time preventing unnecessary energy expenditure and unwanted inhibition of
651 other glomerular columns (i.e. if GABA release would happen from all spines of an
652 activated GC). Thus inactive columns will remain sensitive for new stimuli or changing
653 components because they are not inhibited.
654 In other words, the discovered mechanism allows GCs to perform **lateral inhibition "on**
655 **demand",** selectively on co-active mitral cells, and **thus can provide directed,**
656 **dynamically switched lateral inhibition in a sensory system with 1000 receptor**
657 **channels, therefore explaining the unusual microcircuit of the GC spine/mini-**
658 **neuron as a means of olfactory combinatorial coding.**
659 *Previous evidence for activity-dependence of lateral inhibition and impact of NMDARs*
660 There is substantial prior evidence in the literature for both the activity-dependence and
661 NMDAR-dependence of GC-mediated lateral inhibition. Activity-dependent lateral inhibition
662 was already observed *in vitro* between pairs of MCs; one 'sending' cell was made to fire at a
663 high frequency, whereas the other 'receiving' cell was either not activated at all or subjected
664 to evoked spike trains with increasing frequency (*Arevian et al., 2008*). The receiving MC
665 showed effects of lateral inhibition by the sending MC within a certain range of its own firing,
666 but never for low or no own firing. The authors argue that the activity-dependent effect is due
667 to increased recruitment of firing of interconnecting GCs with increased activity (due to the
668 summation of inputs from both sending and receiving MCs); while such summation can
669 certainly contribute, our results further clarify the reason for a complete lack of lateral
670 inhibition of silent MCs.
671 Yet more importantly, in *in vivo* recordings from MCs there was a subset of MCs that
672 responded exclusively with inhibition to odor activation, presumably via lateral inhibition
673 (*Fukunaga et al., 2014, their Fig 4 and 7)*. However, optogenetic silencing specifically of GCs

674 had no effect whatsoever on this lateral inhibition both in anesthetized and in awake animals,
675 whereas silencing of glomerular inhibitory neurons did. Our results can explain this lack of
676 contribution of GCs to lateral inhibition by the lack of odor-evoked activity in the recorded
677 MCs – thus the presynaptic NMDARs could not be activated and no GC output would occur.
678 A third line of evidence is provided by the fact that markers of neuronal activity (such as c-
679 Fos or 2-deoxyglucose) have revealed the existence of glomerular units/columns spanning
680 all layers of the bulb (e.g. *Kauer & Cinelli 1993*). More recently, retrograde transsynaptic
681 tracing studies using pseudorabies virus injections in the olfactory bulb and piriform cortex
682 have further confirmed this concept, by labeling of subsets of glomerular columns dispersed
683 across the bulb, which very frequently contained a substantial fraction of GCs (*Willhite et al.*
684 *2006, Kim et al. 2011*). The authors already speculated that this patchy labeling could be
685 explained by activity-dependent transsynaptic crossing from MC lateral dendrites, i.e.
686 specifically to active GC spines, which matches with the powered release of GABA restricted
687 to activated columns predicted by our results. Indeed, a recent study has been able to
688 produce compelling evidence for activity-dependent retrograde transsynaptic viral spread
689 (albeit by rabies virus, not pseudorabies; *Beier et al. 2017*). We would predict that
690 interference with GC-NMDAR signalling should prevent the transsynaptic labeling of GCs.
691 Interestingly, *McTavish et al. (2012*) have demonstrated in simulations that columnar arrays
692 of GCs may be particularly effective in mediating synchronization, if the lateral connectivity is
693 symmetric, in line with our hypothesis. To further elucidate this possibility, it would be
694 important to know the impact of more distal GC inputs that were not investigated here for
695 technical reasons. *In vivo*, distal excitation of GCs and accordingly large MC receptive fields
696 have been demonstrated using optical stimulation (*Peace et al. 2017*).
697 As to functional evidence for a strong role of NMDARs in GC-mediated lateral inhibition,
698 NMDAR blockade is routinely used to dissect lateral inhibition in the glomerular layer from
699 GC-mediated lateral inhibition *(Shao et al. 2012, Najac et al. 2015, Geramita & Urban 2017)*.
700 NMDARs play a crucial role in enabling supralinear dendritic integration in GCs, efficiently
701 lowering the threshold for global spiking and thus also for lateral inhibition (*Mueller & Egger*
702 *2020*). Both GC NMDARs and Na_vs are known to play a role specifically in discriminations
703 between binary odorant mixtures in mice, since in the same behavioral paradigm GC-specific

704 knock-down (in about ~ 50% of GCs) of the NMDAR-subunit GluN1 resulted in an increase in
705 discrimination time of on average ~ 60 ms, and knock-down of Na_vs of ~ 85 ms versus
706 control, while discriminations between pure odors were not affected (*Abraham et al., 2010;*
707 *Nunes & Kuner 2018*). These similar effects are in line with our findings, since both
708 modifications should prevent both recurrent and lateral inhibition. However, the relative
709 impact of recurrent inhibition versus lateral inhibition is not known.
710 Moreover, while there is first evidence for substantial dendritic Ca^{2+} signals and local GC
711 spine signals *in vivo* (*Wienisch & Murthy 2016; Wallace et al. 2017; Zhang et al. 2016*), the
712 extent to which specifically local GABA release from GC spines contributes to odor
713 processing in the olfactory bulb is difficult to estimate at this point. Future methodological
714 advances will be required to tackle the contribution of the GC spine spike along with its
715 cooperative release mechanism to bulbar processing, including voltage-sensitive dye
716 imaging and novel genetic loss-of-function approaches for dissecting local recurrent release
717 from lateral inhibition - perhaps by targeting specifically presynaptic NMDARs.
718 *Conclusion: The purpose of the reciprocal spine*
719 In summary, we suggest that reciprocal spines allow the granule cell to selectively interact
720 with coactive glomerular columns. Thus, the reciprocal spine might be a circuit motif that
721 specifically enables efficient binding of dispersed olfactory representations, a coding task that
722 this sensory modality needs to perform due to its large number of receptors. In other words,
723 reciprocal spines with their unique synaptic arrangement and functionality, including spine
724 spikes and presynaptic NMDARs, represent a special adaptation to the demands of sensory
725 processing in the bulb.
726 Another intriguing yet more speculative potential function of target-activity-dependent output
727 is that concurrent preactivation from glutamatergic cortical inputs onto reciprocal spines
728 (ultrastructure in *Price & Powell 1970*) can also enable or enhance lateral inhibition (in
729 addition to providing feed-forward inhibition), allowing for a top-down projection of olfactory
730 templates as has been proposed by *Zelano et al. (2011*).
731

732 **Methods**

733 *Animal handling, slice preparation and electrophysiology*

734 Animals used in our experiments were juvenile Wistar or VGAT-Venus transgenic rats
735 (VGAT-Venus /w-Tg(SLc32a1-YFP*)1Yyan) of either sex (P11 – P19). VGAT-Venus
736 transgenic rats are based on mouse BAC transgenic lines. They were generated by Drs. Y.
737 Yanagawa, M. Hirabayashi and Y. Kawaguchi at the National Institute for Physiological
738 Sciences, Okazaki, Japan, using pCS2-Venus provided by Dr. A. Miyawaki (*Uematsu et al.,*
739 *2008*), RRID: RGD_2314361. In this rat line, fluorescent Venus protein is preferentially
740 expressed in cells carrying the vesicular GABA transporter (VGAT), i.e. GABAergic neurons:
741 the localization of Venus-labeled cells across OB layers was found to be similar to that of
742 GABA-positive cells; direct colocalization in the cortex yielded an overlap of 97% (*Uematsu*
743 *et al., 2008*).

744 Sagittal olfactory bulb brain slices (thickness 300 µm) were prepared in ACSF (composition
745 see below) following procedures in accordance with the rules laid down by the EC Council
746 Directive (86/89/ECC) and German animal welfare legislation. Slices were incubated a water
747 bath at 33°C for 30 min and then kept at room temperature (22°C) until recordings were
748 performed.

749 Olfactory bulb mitral cells were visualized by gradient contrast and recorded from in whole
750 cell voltage clamp mode (at -70 mV or +10 mV) or current clamp mode. Recordings were
751 made with an EPC-10 amplifier and Patchmaster v2.60 software (both HEKA Elektronik,
752 Lambrecht/Pfalz, Germany). Experiments were performed at room temperature (22°C).
753 Patch pipette resistance ranged from 5-6-MΩ. Mitral cells clamped at -70 mV were filled with
754 intracellular solution containing the following substances (in mM): (1) tip solution: 130 K-
755 Methylsulfate, 10 HEPES, 4 MgCl2, 2 Ascorbic acid, 10 Phosphocreatine-di-tris-salt, 2.5
756 Na2ATP, 0.4 NaGTP (2) backfilling solution: 110 Cs-Chloride, 10 HEPES, 10 TEA, 4MgCl2,
757 2 Ascorbic acid, 10 5-N-(2,6-dimethylphenylcarbamoylmethyl) triethylammonium bromide
758 (QX-314, Sigma), 0.2 EGTA, 10 Phosphocreatine, 2.5 Na2ATP, 0.4 NaGTP. Mitral cells
759 clamped at + 10 mV contained internal solution composed of: 125 Cs-methanesulfonate 1
760 NaCl, 0.5 EGTA, 10 HEPES, 3 MgATP, 0.3 NaGTP, 10 Phosphocreatine-di-Tris-salt, 10 QX-

761 314, 0.05 Alexa 594 (Ca^{2+} indicator, Thermofisher Scientific, Waltham. Massachusetts, US),
762 at pH 7.3.
763 For current clamp experiments the internal solution contained: 130 K-Methylsulfate, 10
764 HEPES, 4 MgCl2, 2 Ascorbic acid, 10 Phosphocreatine-di-Tris-salt, 2.5 Na2ATP, 0.4
765 NaGTP. Single APs were evoked by somatic current injection (3 ms, 1 nA) and 5 APs were
766 elicited for every recording condition. Cells with leak currents > 200 pA (at V_{hold} = - 70 mV)
767 were discarded. We chose a hyperpolarized holding potential in order to reduce the
768 activation of NMDA autoreceptors on MC lateral dendrites.
769 The extracellular ACSF was bubbled with carbogen and contained (in mM): 125 NaCl, 26
770 $NaHCO_3$, 1.25 NaH_2PO_4, 20 glucose, 2.5 KCl, 1 $MgCl_2$, and 2 $CaCl_2$. The following
771 pharmacological agents were bath-applied in some experiments: bicucculline (BCC, 50 µM,
772 Sigma-Aldrich), ω-conotoxin MVIIC (CTX, 1 µM, Alomone, Jerusalem, Israel), TTX (500 nM,
773 Alomone), D-APV (25 µM, Tocris), gabazine (GBZ, 20 µM, Tocris). In pharmacological
774 experiments we waited for 10 minutes after wash-in of the drugs TTX, APV resp. CTX. In
775 CTX experiments 1mg/ml cyctochrome C was added to the ACSF. TTX voltage clamp
776 experiments were conducted at clamping potentials of -70 mV (n = 5) or + 10 mV (n = 7),
777 whereas all CTX and APV voltage clamp experiments were conducted at + 10 mV.
778 *Combined two-photon imaging and uncaging*
779 Imaging and uncaging were performed on a Femto-2D-uncage microscope (Femtonics,
780 Budapest, Hungary). Two tunable, Verdi-pumped Ti:Sa lasers (Chameleon Ultra I and II
781 respectively, Coherent, Santa Clara, CA, USA) were used in parallel. The first laser was set
782 either to 900 nm for simultaneous excitation of YFP and Alexa 594 in one channel for
783 visualization of spines and the mitral cell for urIPSC recordings, and the second laser was
784 set to 750 nm for uncaging of caged glutamate. The two laser lines were directly coupled into
785 the pathway of the microscope with a polarization cube (PBS102, Thorlabs Inc, Newton, NJ,
786 USA) and two motorized mirrors. As caged compound we used DNI-caged glutamate (DNI;
787 Femtonics). DNI was used in 1 mM concentration in a closed perfusion circuit with a total
788 volume of 12 ml. Caged compounds were washed in for at least 10 minutes before starting
789 measurements. The uncaging laser was switched using an electro-optical modulator

790 (Pockels cell model 350-80, Conoptics, Danbury, CT, USA). The emitted fluorescence was
791 split into a red and a green channel with a dichroic mirror.

792 Triggering of mitral cell reciprocal IPSCs

793 The region of interest on a proximal lateral mitral cell dendrite was moved to the center of the
794 scanning field. In some initial experiments, four uncaging spots were placed in close
795 apposition along the lateral mitral cell dendrite in case of 'blind' uncaging (n = 8 out of total
796 number of successful experiments n = 44). In most experiments, a single uncaging spot was
797 positioned near the region of interest, using YFP fluorescence of GABAergic cells in VGAT-
798 Venus rats as an optical guide to identify potential synaptic contacts between MC lateral
799 dendrites and GC spines.

800 The parameter settings for two-photon uncaging were as established previously on the same
801 experimental rig for precise mimicking of unitary synaptic Ca^{2+} transients in GC spines
802 (*Egger et al. 2005; Bywalez et al. 2015*). These parameter settings were routinely verified in
803 parallel test experiments, where we imaged Ca^{2+} transients in GC spines following TPU (as
804 in *Bywalez et al. 2015)*. The uncaging site was usually chosen within the top 10-30 µm below
805 the slice surface (since otherwise the visibility of spines in the Venus-VGAT rats was
806 compromised) and the uncaging power was adjusted to the depth of the uncaging site,
807 corresponding to a laser power of approximately 15 mW at the uncaging site (*Sobczyk et al.*
808 *2005*). The uncaging beam was positioned at ~ 0.2 - 0.5 µm distance from the MC
809 dendrite/GC spine head. The uncaging pulse duration was 1 ms. The scanning position was
810 readjusted if necessary before each measurement to account for drift. The microscope was
811 equipped with a 60x Nikon Fluor water immersion objective (NA 1.0; Nikon Instruments,
812 Tokyo, Japan). The microscope was controlled by MES v.5.3190 software (Femtonics). To
813 prevent overstimulation, the uncaging laser power was **not** increased if there was no
814 detectable response. While we cannot exclude overstimulation per se, we would like to argue
815 that systematic overstimulation is unlikely to have occurred based on the following
816 observations (see also Results):

817 - size of urIPSCs as compared to spontaneous activity (Fig. 1F)
818 - low reciprocal release probability from the spine (Fig. 1F)

819 - no extended asynchronous release compared to the classical experiments on
820 recurrent inhibition (mean total duration of TPU-evoked recurrent inhibition ~ 200 ms,
821 Fig. S1E, vs a mean half duration ~ 500 ms in e.g. *Schoppa et al. 1998, Isaacson*
822 *2001*)
823 - no evidence for toxicity in our stability experiments (Fig. 1E)
824 - main finding of dependency of recurrent inhibition on NMDAR activation confirmed by
825 method that does not involve uncaging
826 *Uncaging stability*
827 To test for the stability of uncaging evoked recurrent IPSCs in MCs, uncaging at a dendritic
828 region of interest was performed. If repeated uncaging led to the apparent occurrence of
829 urIPSCs within the same time window (see below for anlysis details), the stability
830 measurement was continued by either uncaging 30 times in total with a frequency of 0.033
831 Hz (every 30 s) or 5 times in a row with 0.033 Hz followed by a 10 min break (to mimic the
832 time for wash-in of pharmacological compounds) and another round of uncaging (5x,
833 0.033Hz). urIPSC amplitudes were taken from averages of the first 5 – 10 and the last 5 – 10
834 uncaging sweeps and statistically compared with each other.
835 *Electrophysiology: Data analysis and statistics*
836 Electrophysiological data were analysed with custom written macros in Igor pro
837 (Wavemetrics, Lake Oswego, OR, USA). Additional sIPSC and urIPSC analysis was
838 performed using the MiniAnalysis program (Synaptosoft, Decature, GA, USA) and Origin
839 (Northampton, MA, USA).
840 <u>Detection of urISPCs</u> Due to the high spontaneous activity, in order to test for the presence
841 of a signal we performed first an area and event analysis of IPSC traces (see below and Fig.
842 1D; if a signal was detected based on these analyses, we went on to search for individual
843 triggered urIPSCs by visual inspection of an overlay of the recorded traces. Individual IPSCs
844 were considered as uncaging-evoked when they repetitively occurred within the same time
845 window (width 3 ± 2 ms, n = 35) after uncaging and had similar kinetics (indicating a similar
846 location of the respective input on the dendrite). Signal types ranged from single urIPSC

events to barrages of urIPSCs lasting tens to hundreds of ms. The release probability was estimated based on 5 – 30 TPU samplings with a mean of 7.5 ± 1.7 stimulations (n = 44).

Area analysis The area was measured in individual traces as the integrated activity above baseline for a 500 ms pre-uncaging baseline window and for a 500 ms post-uncaging window, in order to screen for the presence of a signal (Fig. 1D). The 500 ms extent of the time windows was validated by our measurements of averaged barrage duration (see Fig. S1D2).

Delta (Δ) area values were calculated by subtracting the area of the 500 ms pre-uncaging baseline window ('pre') from the 500 ms post-uncaging window ('post'), in order to isolate the amount of uncaging-evoked inhibitory activity from spontaneous activity. If this procedure was applied to averaged traces and the result was negative, the Δ_area value was set to zero (i.e. no uncaging-evoked activity). While this procedure might still generate false positives due to spontaneous bursts of activity in the post-uncaging window, it also prevents a spurious cancelling of activity (false negative) that otherwise might happen upon averaging Δ_area across an entire set of experiments. Δ_area values for pharmacological conditions were normalized to control Δ_area in order to assess the net effect of drugs on uncaging-evoked inhibitory activity (Fig. 2D, 3D, 4D).

Event analysis Within the individual recorded traces, the peak time points of individual IPSCs were analysed. Peak search parameters in MiniAnalysis were adjusted in order to detect potentially all IPSCs within a trace. For detailed spontaneous IPSC amplitude analysis, IPSCs were sorted manually after the automated peak search and discarded if the amplitude exceeded less than 5 pA and/or the IPSC onset was not be detected properly. Event counts were averaged for the 500 ms pre-uncaging and the 500 ms post-uncaging windows, respectively.

Evaluation of effects of pharmacological agents For determining drug effects, the averaged urIPSC amplitudes were scaled down by the ratio of number of responses to total number of trials, both in control and drug condition, in order to account also for changes in release probability. If no single responses/urIPSCs could be detected anymore in the presence of TTX, CTX or APV according to the criteria described above, we measured the mean amplitude of V_m above baseline in the averaged response at the time point of the maximal

877 response amplitude in control condition. If this value was below 0, the response size was set
878 to 0 pA. If the value was larger than 0, we interpreted it as average drug response amplitude
879 including failures and thus did not scale it. This conservative method prevents false
880 negatives due to lacking sensitivity in individual trials in the presence of the drug.
881 Detection of spontaneous activity Spontaneous IPSCs were recorded prior to wash-in of DNI,
882 in the presence of DNI and in the presence of each pharmacological compound. For each
883 condition, data were analysed for a total duration of 20 s of recordings.
884 Analysis of afterhyperpolarizations All stable MC AP recordings within either baseline or drug
885 condition were averaged (n = 5 each). If between the two conditions the holding membrane
886 potential changed by more than 0.3 mV, or the time course (onset of upstroke relative to
887 onset of step depolarization, width) and/or the amplitude of the AP changed by more than
888 15% from their baseline values, the experiment was discarded. If single individual recordings
889 showed such variations, they were not included in the average. For each average, the AHP
890 amplitude was measured as the maximal negative deflection of the membrane potential from
891 the resting membrane potential.
892 *Simulations*
893 The simulations are based on a published compartmental model in NEURON (Aghvami et
894 al., 2019, ModelDB entry 244687). This model uses the 5-state gating model for NMDA
895 receptors (*Destexhe et al. 1998*), while the HVACC model is adopted from *Hemond et al.*
896 *2008,* with adjustments based on own Ca^{2+} current recordings (see *Aghvami et al. 2019*). For
897 the simulations shown in Fig. 5, there was no exogenous Ca^{2+} buffer included except for
898 panel E where fluorescence transients were simulated in the presence of 100 µM of the
899 Ca^{2+}-sensitive dye OGB-1 in order to emulate the experimental situation from *Bywalez et al.*
900 *2015*.
901 As a readout measure for the temporal overlap between I_{Ca_NMDAR} and I_{Ca_HVACC} we first
902 determined the FWHM (full width half maximum) for each current and then the interval within
903 which the two FWHMs overlapped. At this point, we focussed on temporal relationships and
904 did not account for current amplitudes or integrals, since Ca^{2+} concentration changes within
905 nanodomains cannot be properly simulated in NEURON and thus spine Ca^{2+} current
906 amplitudes are of limited meaning. We tested for the robustness of this measure

907 against variation of those model parameters that are crucially involved in the generation of
908 the spine spike, i.e. the resistance of the spine neck (R_{neck}), the conductance of AMPA
909 receptors (g_{AMPA}) and the voltage-gated sodium channel conductance (varied in proportion to
910 the potassium channel conductance, $g_{Na/K}$). Their nominal values in the GC model are 1.7
911 GΩ, 2000 pS and 0.5 S/cm^2 respectively. Each parameter was varied between up to 200% of
912 the nominal value, and down until no spine spike was generated any more.

913 *Immunogold labeling and electron microscopy*

914 Immunogold labeling was performed on cryosubstituted rat olfactory bulbs (n = 4 animals, 3
915 months old), that had been used previously; for further details on the fixation, embedding and
916 immunogold labeling procedure see (*Sassoè-Pognetto & Ottersen, 2000; Sassoè-Pognetto*
917 *et al., 2003*).

918 To maximize detection of the GluN1 subunit, we used a combination of two rabbit antisera as
919 described in *Sassoè-Pognetto et al. (2003)*. One antiserum (kindly donated by Anne
920 Stephenson) binds an extracellular domain (amino acid residues 17–35) common to all splice
921 variants of the GluN1 subunit (*Chazot et al. 1995; Racca et al. 2000*). The other antiserum
922 was raised against a C-terminal domain and recognizes four splice variants (Chemicon,
923 Temecula, CA; catalog No. AB1516).

924 For GluN2, we used a affinity-purified rabbit antibody raised against a synthetic peptide
925 corresponding to the C-terminus of the GluN2A subunit conjugated to BSA (Chemicon, cat.
926 no. AB1548). According to the manufacturer, this antibody recognizes the GluN2A and
927 GluN2B subunits in Western blot analysis of transfected cells.

928 *Ultrastructure data analysis and statistics*

929 Grid squares were analysed systematically for the presence of synaptic profiles (symmetric
930 and/or asymmetric) between GC spines and MC dendrites (Fig. 6; see also Fig. 1A in
931 *Sassoè-Pognetto & Ottersen 2000*). Synaptic profiles were then photographed at high
932 magnification (75.000 - 120.000x) with a side-mounted CCD camera (Mega View III,
933 Olympus Soft Imaging System). The plasma membrane of GC spines, when clearly visible,
934 was classified as either belonging to an asymmetric synaptic profile, a symmetric profile, or a
935 non-synaptic segment (see Fig. 6A2 for examples). The length of segments was measured
936 along the spine membrane curvature (using ImageJ 1.52 analysis software) and the number

937 of immunogold particles within a distance of ≤ 30 nm from the GC spine membrane was
938 counted for the individual segments. The lengths of non-synaptic segments were on average
939 longer than those of synaptic segments, which argues against an undersampling of gold
940 particle densities in non-synaptic membranes compared to synaptic membranes and thus a
941 false positive difference between the density distribution in non-synaptic membranes and
942 symmetric profiles (GluN1: mean non-synaptic segment length: 610 ± 400 nm, n = 138,
943 symmetric synaptic profiles: 270 ± 120 nm, n = 120, asymmetric synaptic profiles: 260 ± 110
944 nm, n = 111; similar results for GluN2, not shown). When both symmetric and asymmetric
945 synaptic profiles were visible in the same individual spine, the distance of such reciprocal
946 contacts was also measured along the curvature of the GC spine membrane.
947 The distribution of labeling along the axis perpendicular to the GC spine membrane (radial
948 axis) was determined by examining micrographs of transversely cut synaptic profiles, with
949 well defined presynaptic and postsynaptic membranes. Here all particles at distances up to
950 40 µm were counted to prevent a possible bias.
951 *Statistical tests*
952 All electrophysiological data were analysed with non-parametric paired (*Wilcoxon matched*
953 pairs) or unpaired (*Mann-Whitney-U*) tests and expressed as mean ± SD. The density
954 distributions of immunogold particles were compared with the Kolmogorov-Smirnov test
955 (https://www.wessa.net/rwasp_Reddy-Moores%20K-S%20Test.wasp).
956
957 ***Author contributions***
958 VLR performed all uncaging experiments. LZ performed MC current clamp recordings. VLR,
959 GB, MSP and VE analyzed data. SSA performed simulations. VE and VLR designed
960 research and wrote the manuscript, with MSP contributing to the parts on ultrastructure. BR
961 provided DNI-caged glutamate and assisted in editing the manuscript.

962 ***Acknowledgments***
963 We thank Anne Pietryga-Krieger for expert technical assistance, Marius Stephan and Philipp
964 Seidel for assistance with IPSC analysis, Gagik Yeghiazaryan for initial MC current clamp
965 recordings, Imre Vida for facilitating access to VGAT-Venus rats, Sigrun Korsching and
966 Yoshiyuki Kubota for advice on statistics and Ursula Koch for advice on pharmacology and

discussions on lateral inhibition. This work was funded mainly by the German Federal Ministry for Education and Research (BMBF, 01GQ1104/01GQ1502), with additional equipment funding by LMU-GSN, DFG-SFB 870 and funding for staff from GIF (1479-418.13; all to VE), and by ERC 682426, GINOP_2.1.1-15-2016-00979, VKSZ_14-1-2015-0155, 712821-NEURAM to BR.

Competing interests

There are competing financial interests since BR is a founder of Femtonics Kft and a member of its scientific advisory board. No other competing interests exist.

976 ***References***

977 1. Abraham, N. M., Egger, V., Shimshek, D. R., Renden, R., Fukunaga, I., Sprengel, R.,
978 Seeburg, P. H., Klugmann, M., Margrie, T. W., Schaefer, A. T., & Kuner, T. (2010). Synaptic
979 inhibition in the olfactory bulb accelerates odor discrimination in mice. *Neuron, 65*(3), 399-
980 411.
981 2. Aghvami, S., Müller, M., Araabi ,B.N., & Egger V. (2019) Coincidence detection within the
982 excitable rat olfactory bulb granule cell spines. *J. Neurosci*. 39, 584-595. doi:
983 10.1523/JNEUROSCI.1798-18.2018
984 3. Angelo, K., & Margrie, T. W. (2011). Population diversity and function of hyperpolarization-
985 activated current in olfactory bulb mitral cells. *Sci Rep, 1*, 50. doi:10.1038/srep00050
986 4. Arevian A.,C., Kapoor, V., Urban, N.N. (2008). Activity-dependent gating of lateral inhibition
987 in the mouse olfactory bulb. *Nat Neurosci* 11, 80-87.
988 5. Arnson, H. A., & Strowbridge, B. (2017). Spatial Structure Of Synchronized Inhibition In The
989 Olfactory Bulb. *J Neurosci,* 37(43):10468 –10480. doi:10.1523/JNEUROSCI.1004-17.2017
990 6. Banerjee, A., Larsen, R.S., Philpot, B.D., & Paulsen,O. (2016). Roles of Presynaptic NMDA
991 Receptors in Neurotransmission and Plasticity. *Trends in Neurosciences* 39 (1).
992 http://dx.doi.org/10.1016/j.tins.2015.11.001
993 7. Bartel, D. L., Rela, L., Hsieh, L., & Greer, C. A. (2015). Dendrodendritic synapses in the
994 mouse olfactory bulb external plexiform layer. *J Comp Neurol, 523*(8), 1145-1161.
995 doi:10.1002/cne.23714
996 8. Beier KT, Kim CK, Hoerbelt P, Hung LW, Heifets BD, DeLoach KE, Mosca TJ, Neuner S,
997 Deisseroth K, Luo L, Malenka RC. (2017) Rabies screen reveals GPe control of cocaine-
998 triggered plasticity. Nature 549, 345-350. doi: 10.1038/nature23888.
999 9. Bloodgood, B. L., & Sabatini, B. L. (2007). Ca(2+) signaling in dendritic spines. *Curr Opin*
1000 *Neurobiol, 17*(3), 345-351. doi:10.1016/j.conb.2007.04.003
1001 10. Bouvier, G., Bidoret, C., Casado, M., & Paoletti, P. (2015). Presynaptic NMDA receptors:
1002 Roles and rules. *Neuroscience, 311*, 322-340. doi:10.1016/j.neuroscience.2015.10.033
1003 11. Brea JN, Kay LM, Kopell NJ. (2009). Biophysical model for gamma rhythms in the olfactory
1004 bulb via subthreshold oscilations. *Proc Natl Acad Sci U S A,* 106, 21954-9. doi:
1005 10.1073/pnas.0910964106.
1006 12. Burton SD. (2017). Inhibitory circuits of the main olfactory bulb. J Neurophysiol. 2017 Oct
1007 1;118(4):2034-2051. doi: 10.1152/jn.00109.2017
1008 13. Bywalez, W. G., Patirniche, D., Rupprecht, V., Stemmler, M., Herz, A. V. M., Pálfi, D., Rozsa,
1009 B., & Egger, V. (2015). Local Postsynaptic Voltage-Gated Sodium Channel Activation in
1010 Dendritic Spines of Olfactory Bulb Granule Cells. *Neuron, 85*(3), 590-601.
1011 doi:10.1016/j.neuron.2014.12.051
1012 14. Carlson, G. C., Shipley, M. T., & Keller, A. (2000). Long-lasting depolarizations in mitral cells
1013 of the rat olfactory bulb. *J Neurosci, 20*(5), 2011-2021.
1014 15. Chae H, Kepple DR, Bast WG, Murthy VN, Koulakov AA, Albeanu DF. (2019). Mosaic

1015 representations of odors in the input and output layers of the mouse olfactory bulb. Nat
1016 Neurosci. 22:1306-1317. doi: 10.1038/s41593-019-0442-z.
1017 16. Chazot, P.L., Cik, M., & Stephenson, F.A. (1995). An investigation into the role of N-
1018 glycosylation in the functional expression of a recombinant heteromeric NMDA receptor. Mol
1019 Membr Biol, 12,331-337.
1020 17. Chen, W. R., Xiong, W., & Shepherd, G. M. (2000). Analysis of relations between NMDA
1021 receptors and GABA release at olfactory bulb reciprocal synapses. *Neuron, 25*(3), 625-633.
1022 18. Chiovini, B., Turi, G. F., Katona, G., Kaszas, A., Palfi, D., Maak, P., Szalay, G., Szabo, M. F.,
1023 Szabo, G., Szadai, Z., Kali, S., & Rozsa, B. (2014). Dendritic spikes induce ripples in
1024 parvalbumin interneurons during hippocampal sharp waves. *Neuron, 82*(4), 908-924.
1025 doi:10.1016/j.neuron.2014.04.004
1026 19. Cleland TA, Sethupathy P. (2006) Non-topographical contrast enhancement in the
1027 olfactory bulb. BMC Neurosci. 24,7:7.
1028 20. Crespo, C., Liberia, T., Blasco-Ibáñez, J.M., Nácher, J., & Varea, E. (2013). The circuits of
1029 the olfactory bulb. The exception as a rule. Anat Rec (Hoboken)., 296(9):1401-1412. doi:
1030 10.1002/ar.22732.
1031 21. Destexhe, A., Mainen, Z.F., & Sejnowski, T.J. (1998). Kinetic models of synaptic
1032 transmission. In: Methods in Neuronal Modeling (2nd edition; edited by Koch, C., & Segev,
1033 I.). MIT press, Cambridge, 1998, 1-25.
1034 22. Duguid, I., & Smart, T.G. (2004) Retograde activation of presynaptic NMDA receptors
1035 enhances GABA release at cerebellar interneuton-Purkinje cell synapses. *Nat Neurosci*, 7(5),
1036 525-533.
1037 23. Duménieu, M., Fourcaud-Trocmé, N., Garcia, S., & Kuczewski, N. (2015).
1038 Afterhyperpolarization (AHP) regulates the frequency and timing of action potentials in the
1039 mitral cells of the olfactory bulb: role of olfactory experience. Physiol Rep, 3(5). pii: e12344.
1040 doi: 10.14814/phy2.12344.
1041 24. Economo MN, Hansen KR, Wachowiak M (2016) Control of Mitral/Tufted Cell Output by
1042 Selective Inhibition among Olfactory Bulb Glomeruli. Neuron 91, 397-411.
1043 25. Egger, V. (2008). Synaptic sodium spikes trigger long-lasting depolarizations and slow
1044 calcium entry in rat olfactory bulb granule cells. *Eur J Neurosci, 27*(8), 2066-2075.
1045 26. Egger, V., Svoboda, K., & Mainen, Z. F. (2003) Mechanisms of lateral inhibition in the
1046 olfactory bulb: efficiency and modulation of spike-evoked calcium influx into granule cells. J
1047 Neurosci 23:7551–7559.
1048 27. Egger, V., Svoboda, K., & Mainen, Z. F. (2005). Dendrodendritic synaptic signals in olfactory
1049 bulb granule cells: Local spine boost and global low-threshold spike. *J Neurosci, 25*, 3521-
1050 3530.
1051 28. Egger, V., & Urban, N. N. (2006). Dynamic connectivity in the mitral cell-granule cell
1052 microcircuit. *Semin Cell Dev Biol, 17*(4), 424-432.
1053 29. Fantana AL, Soucy ER & Meister M (2008) Rat Olfactory Bulb Mitral Cells Receive Sparse

1054 Glomerular Inputs. Neuron 59, 802–814.
1055 30. Friedman, D., & Strowbridge, B. W. (2000). Functional role of NMDA autoreceptors in
1056 olfactory mitral cells. *J Neurophysiol, 84*(1), 39-50. doi:10.1152/jn.2000.84.1.39
1057 31. Fukunaga, I., Herb, J. T., Kollo, M., Boyden, E. S., & Schaefer, A. T. (2014). Independent
1058 control of gamma and theta activity by distinct interneuron networks in the olfactory bulb. *Nat*
1059 *Neurosci, 17*(9), 1208-1216. doi:10.1038/nn.3760
1060 32. Geramita M, Urban NN. (2017) Differences in Glomerular-Layer-Mediated Feedforward
1061 Inhibition onto Mitral and Tufted Cells Lead to Distinct Modes of Intensity Coding. J Neurosci.
1062 2017 Feb 8;37(6):1428-1438.
1063 33. Glitsch, M., & Marty, A. (1999). Presynaptic Effects of NMDA in Cerebellar Purkinje Cells and
1064 Interneurons. J Neurosci, 19(2):511-519.
1065 34. Grunditz, Å., Holbro, N., Tian, L., Zuo, Y., & Oertner, T.G. (2008). Spine Neck Plasticity
1066 Controls Postsynaptic Calcium Signals through Electrical Compartmentalization. J Neurosci
1067 28:13457-13466.
1068 35. Halabisky, B., Friedman, D., Radojicic, M., & Strowbridge, B. W. (2000). Calcium influx
1069 through NMDA receptors directly evokes GABA release in olfactory bulb granule cells. *J*
1070 *Neurosci, 20*(13), 5124-5134.
1071 36. Hemond, P., Epstein, D., Boley, A., Migliore, M., Ascoli, G.A., & Jaffe, D.B. (2008). Distinct
1072 classes of pyramidal cells exhibit mutually exclusive firing patterns in hippocampal area
1073 CA3b. *Hippocampus* 18:411-424.
1074 37. Huang, L., Garcia, I., Jen, H.-I., & Arenkiel, B. R. (2013). Reciprocal connectivity between
1075 mitral cells and external plexiform layer interneurons in the mouse olfactory bulb. *Frontiers in*
1076 *Neural Circuits, 7*. doi:10.3389/fncir.2013.00032
1077 38. Isaacson, J. S. (1999). Glutamate spillover mediates excitatory transmission in the rat
1078 olfactory bulb. *Neuron, 23*(2), 377-384.
1079 39. Isaacson, J. S. (2001). Mechanisms governing dendritic gamma-aminobutyric acid (GABA)
1080 release in the rat olfactory bulb. *Proc Natl Acad Sci U S A, 98*(1), 337-342.
1081 40. Isaacson, J. S., & Strowbridge, B. W. (1998). Olfactory reciprocal synapses: dendritic
1082 signaling in the CNS. *Neuron, 20*(4), 749-761.
1083 41. Jackowski A, Parnavelas JG, Lieberman AR. (1978) The reciprocal synapse in the external
1084 plexiform layer of the mammalian olfactory bulb. Brain Res. 1978 Dec 22;159(1):17-28. doi:
1085 10.1016/0006-8993(78)90106-3.
1086 42. Kaeser, P. S., & Regehr, W. G. (2014). Molecular mechanisms for synchronous,
1087 asynchronous, and spontaneous neurotransmitter release. *Annu Rev Physiol, 76*, 333-363.
1088 doi:10.1146/annurev-physiol-021113-170338
1089 43. Kampa, B., Clements, J., Jonas, P., & Stuart, G.J. (2004) Kinetics of Mg2+ unblock of NMDA
1090 receptors: implications for spike-timing dependent synaptic plasticity. J Physiol, 556.2, 337-
1091 345.
1092 44. Kapoor, V., & Urban, N. N. (2006). Glomerulus-specific, long-latency activity in the olfactory

1093 bulb granule cell network. *J Neurosci, 26*, 11706-11719.
1094 45. Kashiwadani H, Sasaki YF, Uchida N, Mori K. (1999) Synchronized oscillatory discharges of
1095 mitral/tufted cells with different molecular receptive ranges in the rabbit olfactory bulb. J
1096 Neurophysiol. 82(4):1786-92.
1097 46. Kato, H. K., Gillet, S. N., Peters, A. J., Isaacson, J. S., & Komiyama, T. (2013). Parvalbumin-
1098 expressing interneurons linearly control olfactory bulb output. *Neuron, 80*(5),
1099 10.1016/j.neuron.2013.1008.1036. doi:10.1016/j.neuron.2013.08.036
1100 47. Kauer J.S. & Cinelli A.R. Are there structural and functional modules in the vertebrate
1101 olfactory bulb? *Microsc. Res. Tech.* **24**, 157-167(1993)
1102 48. Kay, L. M. (2003). Two species of gamma oscillations in the olfactory bulb: dependence on
1103 behavioral state and synaptic interactions. *J Integr Neurosci, 2*(1), 31-44.
1104 49. Khawaled, R., Bruening-Wright, A., Adelman, J. P., & Maylie, J. (1999). Bicuculline Block of
1105 Small-conductance Calcium-activated Potassium Channels. *Pflügers Archiv : Eur J Physiol.*
1106 **438** (3): 314–321. doi:10.1007/s004240050915.
1107 50. Kim DH, Phillips ME, Chang AY, Patel HK, Nguyen KT, Willhite DC. (2011) Lateral
1108 Connectivity in the Olfactory Bulb is Sparse and Segregated. Front Neural Circuits. 25;5:5.
1109 doi: 10.3389/fncir.2011.00005.
1110 51. Lagier, S., Carleton, A., & Lledo, P.-M. (2004). Interplay between Local GABAergic
1111 Interneurons and Relay Neurons Generates Gamma Oscillations in the Rat Olfactory Bulb. *J*
1112 *Neurosci*, 24(18):4382– 4392.
1113 52. Laurent G., Wehr M. & Davidowitz H. (1996) Temporal representations of odors in an
1114 olfactory network. *J. Neurosci.* **16**, 3837-3847 (1996)
1115 53. Lepousez, G., Csaba, Z., Bernard, V., Loudes, C., Videau, C., Lacombe, J., Epelbaum, J., &
1116 Viollet, C. (2010). Somatostatin interneurons delineate the inner part of the external plexiform
1117 layer in the mouse main olfactory bulb. *J Comp Neurol, 518*(11), 1976-1994.
1118 doi:10.1002/cne.22317
1119 54. Lester, R.A., Clements, J.D.,Westbrook, G.L., & Jahr, C.E. (1990) NMDAR Channel kinetics
1120 determine the time course of NMDA receptor-mediated synaptic currents. Nature,
1121 346(6284):565-567.
1122 55. Li A., Gire H.G., & Restrepo D. (2015) Spike-Field Coherence in a Population of Olfactory
1123 Bulb Neurons Differentiates between Odors Irrespective of Associated Outcome. J Neurosci
1124 35(14):5808-5822
1125 56. Matsuno T, Kiyokage E, Toida K. (2017) Synaptic distribution of individually labeled mitral
1126 cells in the external plexiform layer of the mouse olfactory bulb. J Comp Neurol. 525(7):1633-
1127 1648. doi: 10.1002/cne.24148.
1128 57. McGuinness, L., Taylor, C., Taylor, R.D., Yau, C., Langenhan, T., Hart, M.L., Christian, H.,
1129 Tynan, P.W., Donnelly, P., & Emptage, N.J. (2010). Presynaptic NMDARs in the
1130 hippocampus facilitate transmitter release at theta frequency. *Neuron*, 68(6):1109-1127. doi:
1131 10.1016/j.neuron.2010.11.023.

1132 58. McIntyre, A. B. R., & Cleland, T. A. (2016). Biophysical constraints on lateral inhibition in the
1133 olfactory bulb. *Journal of Neurophysiology, 115*(6), 2937-2949. doi:10.1152/jn.00671.2015
1134 59. McTavish TS, Migliore M, Shepherd GM, Hines ML. (2012) Mitral cell spike synchroniy
1135 modulated by dendrodendritic synapse location. Front Comput Neurosci. 6:3. doi:
1136 10.3389/fncom.2012.00003.
1137 60. Miller, J. P., Rall, W., & Rinzel, J. (1985). Synaptic amplification by active membrane in
1138 dendritic spines. *Brain Res, 325*(1-2), 325-330.
1139 61. Miyamichi, K., Shlomai-Fuchs, Y., Shu, M., Weissbourd, B. C., Luo, L., & Mizrahi, A. (2013).
1140 Dissecting Local Circuits: Parvalbumin Interneurons Underlie Broad Feedback Control of
1141 Olfactory Bulb Output. *Neuron, 80*(5), 1232-1245. doi:10.1016/j.neuron.2013.08.027
1142 62. Mori, K., Nagao, H., & Yoshihara, Y. (1999). The olfactory bulb: Coding and Processing of
1143 odor molecule information. *Science*, 286, 711-715.
1144 63. Mueller M**.,** Egger V. (2020) Dendritic integration in olfactory bulb granule cells: Threshold for
1145 lateral inhibition and role of active conductances upon simultaneous activation.
1146 bioRxiv:901397. doi.org/10.1101/2020.01.10.901397
1147 64. Nagayama S, Homma R, Imamura F. (2014) Neuronal organization of olfactory bulb circuits.
1148 Front Neural Circuits. 8:98. doi: 10.3389/fncir.2014.00098.
1149 65. Najac M, Sanz Diez A, Kumar A, Benito N, Charpak S, De Saint Jan D. (2015)
1150 Intraglomerular lateral inhibition promotes spike timing variability in principal neurons of the
1151 olfactory bulb. J Neurosci. 35(10):4319-31. doi: 10.1523/JNEUROSCI.2181-14.2015.
1152 66. Naritsuka, H., Sakai, K., Hashikawa, T., Mori, K., & Yamaguchi, M. (2009). Perisomatic-
1153 targeting Granule Cells in the Mouse Olfactory Bulb. *J Comp Neurol*, 525, 409-426.
1154 67. Nunes, D., & Kuner, T. (2018). Axonal sodium channel NaV1.2 drives granule cell dendritic
1155 GABA release and rapid odor discrimination. *PLoS Biol, 16*(8), e2003816.
1156 doi:10.1371/journal.pbio.2003816
1157 68. Pálfi, D., Chiovini, B., Szalay, G., Kaszás, A., Turi, G.F., Katona, G., Ábrányi-Balogh, P.,
1158 Szőri, M., Potor, A., Frigyesi, O., Lukácsné Haveland, C., Szadai, Z., Madarász, M.,
1159 Vasanits-Zsigrai, A., Molnár-Perl, I., Viskolcz, B., Csizmadia, I.G., Mucsi, Z., & Rózsa, B.
1160 (2018). High efficiency two-photon uncaging coupled by the correction of spontaneous
1161 hydrolysis. Org Biomol Chem. 16(11):1958-1970. doi: 10.1039/c8ob00025e.
1162 69. Peace ST, Johnson BC, Li G, Kaiser ME, Fukunaga I, Schaefer AT, Molnar AC, Cleland TA
1163 (2017) Coherent olfactory bulb gamma oscillations arise from coupling independent columnar
1164 oscillations. bioRxiv 213827; doi: https://doi.org/10.1101/213827
1165 70. Pressler, R. T., & Strowbridge, B. W. (2017). Direct Recording of Dendrodendritic Excitation
1166 in the Olfactory Bulb: Divergent Properties of Local and External Glutamatergic Inputs
1167 Govern Synaptic Integration in Granule Cells. *J Neurosci, 37*(49), 11774-11788.
1168 doi:10.1523/JNEUROSCI.2033-17.2017
1169 71. Pressler, R. T., & Strowbridge, B. W. (2019). Functional specialization of interneuron
1170 dendrites: Identification of action potential initiation zone in axonless olfactory bulb granule

1171 cells. J Neurosci. 39(49):9674-9688. doi: 10.1523/JNEUROSCI.1763-19.2019
1172 72. Price J.L. & Powell T.P. (1970) An experimental study of the origin and the course of the
1173 centrifugal fibres to the olfactory bulb in the rat. *J Anat.* **107**:215-237
1174 73. Racca, C., Stephenson, F.A., Streit, P., Roberts, J.D., & Somogyi, P. (2000). NMDA receptor
1175 content of synapses in stratum radiatum of the hippocampal CA1 area. J Neurosci.
1176 20(7):2512-2522.
1177 74. Rannals, M. D., & Kapur, J. (2011). Homeostatic strengthening of inhibitory synapses is
1178 mediated by the accumulation of GABA(A) receptors. *J Neurosci, 31*(48), 17701-17712.
1179 doi:10.1523/JNEUROSCI.4476-11.2011
1180 75. Sailor, Kurt A., Valley, Matthew T., Wiechert, Martin T., Riecke, H., Sun, Gerald J., Adams,
1181 W., . . . Lledo, P.-M. (2016). Persistent Structural Plasticity Optimizes Sensory Information
1182 Processing in the Olfactory Bulb. *Neuron, 91*(2), 384-396.
1183 doi:http://dx.doi.org/10.1016/j.neuron.2016.06.004
1184 76. Sassoé-Pognetto, M., & Ottersen, O. P. (2000). Organization of Ionotropic Glutamate
1185 Receptors at Dendrodendritic Synapses in the Rat Olfactory Bulb. J Neurosci, 20(6):2192–
1186 2201.
1187 77. Sassoé-Pognetto, M., Utvik, J. K., Camoletto, P., Watanabe, M., Stephenson, F. A., Bredt, D.
1188 S., & Ottersen, O. P. (2003). Organization of postsynaptic density proteins and glutamate
1189 receptors in axodendritic and dendrodendritic synapses of the rat olfactory bulb. *J Comp*
1190 *Neurol, 463*(3), 237-248.
1191 78. Schmidt, L. J., & Strowbridge, B. W. (2014). Modulation of olfactory bulb network activity by
1192 serotonin: synchronous inhibition of mitral cells mediated by spatially localized GABAergic
1193 microcircuits. *Learn Mem, 21*(8), 406-416. doi:10.1101/lm.035659.114
1194 79. Schoppa, N. E., Kinzie, J. M., Sahara, Y., Segerson, T. P., & Westbrook, G. L. (1998).
1195 Dendrodendritic inhibition in the olfactory bulb is driven by NMDA receptors. *J Neurosci,*
1196 *18*(17), 6790-6802.
1197 80. Schoppa NE (2006) AMPA/kainate receptors drive rapid output and precise synchrony in
1198 olfactory bulb granule cells. J Neurosci 26:12996-13006.
1199 81. Shao Z, Puche AC, Liu S, Shipley MT. (2012) Intraglomerular inhibition shapes the strength
1200 and temporal structure of glomerular output. J Neurophysiol. 108(3):782-93. doi:
1201 10.1152/jn.00119.2012.
1202 82. Shepherd GM, Chen WR, Willhite D, Migliore M, Greer CA. (2007) The olfactory granule cell:
1203 From classical enigma to central role in olfactory processing. Brain Res Rev 55, 373-382
1204 83. Sobczyk, A., Scheuss, V., & Svoboda, K. (2005). NMDA receptor subunit-dependent [Ca2+]
1205 signaling in individual hippocampal dendritic spines. *J Neurosci, 25*(26), 6037-6046.
1206 doi:10.1523/JNEUROSCI.1221-05.2005
1207 84. Spruston, N. (2008). Pyramidal neurons: dendritic structure and synaptic integration. *Nat Rev*
1208 *Neurosci, 9*(3), 206-221. doi:10.1038/nrn2286
1209 85. Stanley, E. F. (2016) The Nanophysiology of Fast Transmitter Release. *Trends Neurosci.* 39

1210 (3). http://dx.doi.org/10.1016/j.tins.2016.01.005
1211 86. Stroh O, Freichel M, Kretz O, Birnbaumer L, Hartmann J, Egger V (2012) NMDA-receptor
1212 dependent synaptic activation of TRPC channels in the olfactory bulb. *J Neurosci 32*: 5737–
1213 5746
1214 87. Toida, K., Kosaka, K., Heizmann, C. W., & Kosaka, T. (1994). Synaptic contacts between
1215 mitral/tufted cells and GABAergic neurons containing calcium-binding protein parvalbumin in
1216 the rat olfactory bulb, with special reference to reciprocal synapses between them. *Brain Res,*
1217 *650*(2), 347-352.
1218 88. Tonnesen, J., & Nagerl, U. V. (2016) Dendritic Spines as Tunable Regulators of Synaptic
1219 Signals. *Front Psychiatry* 7:101. doi: 10.3389/fpsyt.2016.00101
1220 89. Uematsu, M., Hirai, Y., Karube, F., Ebihara, S., Kato, M., Abe, K., . . . Kawaguchi, Y. (2008).
1221 Quantitative Chemical Composition of Cortical GABAergic Neurons Revealed in Transgenic
1222 Venus-Expressing Rats. *Cerebral Cortex, 18*(2), 315-330. doi:10.1093/cercor/bhm056
1223 90. Urban N.N. & Arevian A.C. (2009). Computing with dendrodendritic syanpses in the olfactory
1224 bulb. *Ann. N.Y. Acad. Sci. 1*170: 264–269. doi: 10.1111/j.1749-6632.2009.03899.x
1225 91. Veruki, M. L., Zhou, Y., Castilho, A., Morgans, C. W., & Hartveit, E. (2019) Extrasynaptic
1226 NMDA Receptors on Rod Pathway Amacrine Cells: Molecular Composition, Activation, and
1227 Signaling. *J Neurosci* 39: 627-650. Doi: 10.1523/JNEUROSCI.2267-18.2018
1228 92. Wallace, J. L., Wienisch, M., & Murthy, V. N. (2017). Development and Refinement of
1229 Functional Properties of Adult-Born Neurons. *Neuron, 96*(4), 883-896.e887.
1230 doi:10.1016/j.neuron.2017.09.039
1231 93. Wellis, D. P., & Kauer, J. S. (1993). GABAA and glutamate receptor involvement in
1232 dendrodendritic synaptic interactions from salamander olfactory bulb. *J Physiol, 469*, 315-
1233 339.
1234 94. Wienisch, M., & Murthy, V. N. (2016). Population imaging at subcellular resolution supports
1235 specific and local inhibition by granule cells in the olfactory bulb. *Scientific Reports, 6*, 29308.
1236 doi:10.1038/srep29308
1237 95. Willhite DC, Nguyen KT, Masurkar AV, Greer CA, Shepherd GM, Chen WR (2006) Viral
1238 tracing identifies distributed columnar organization in the olfactory bulb. PNAS 103:12592-
1239 12597.
1240 96. Woolf, T. B., Shepherd, G. M., & Greer, C. A. (1991). Serial reconstructions of granule cell
1241 spines in the mammalian olfactory bulb. *Synapse, 7*(3), 181-192.
1242 97. Zelano C, Mohanty A, Gottfried JA. (2011) Olfactory predictive codes and stimulus templates
1243 in piriform cortex. Neuron. 72(1):178-87. doi: 10.1016/j.neuron.2011.08.010.
1244 98. Zhang, L., Huang, Y., & Hu, B. (2016). Olfactory experiences dynamically regulate plasticity
1245 of dendritic spines in granule cells of Xenopus tadpoles in vivo. *Scientific Reports, 6*, 35009.
1246 doi:10.1038/srep35009
1247
1248

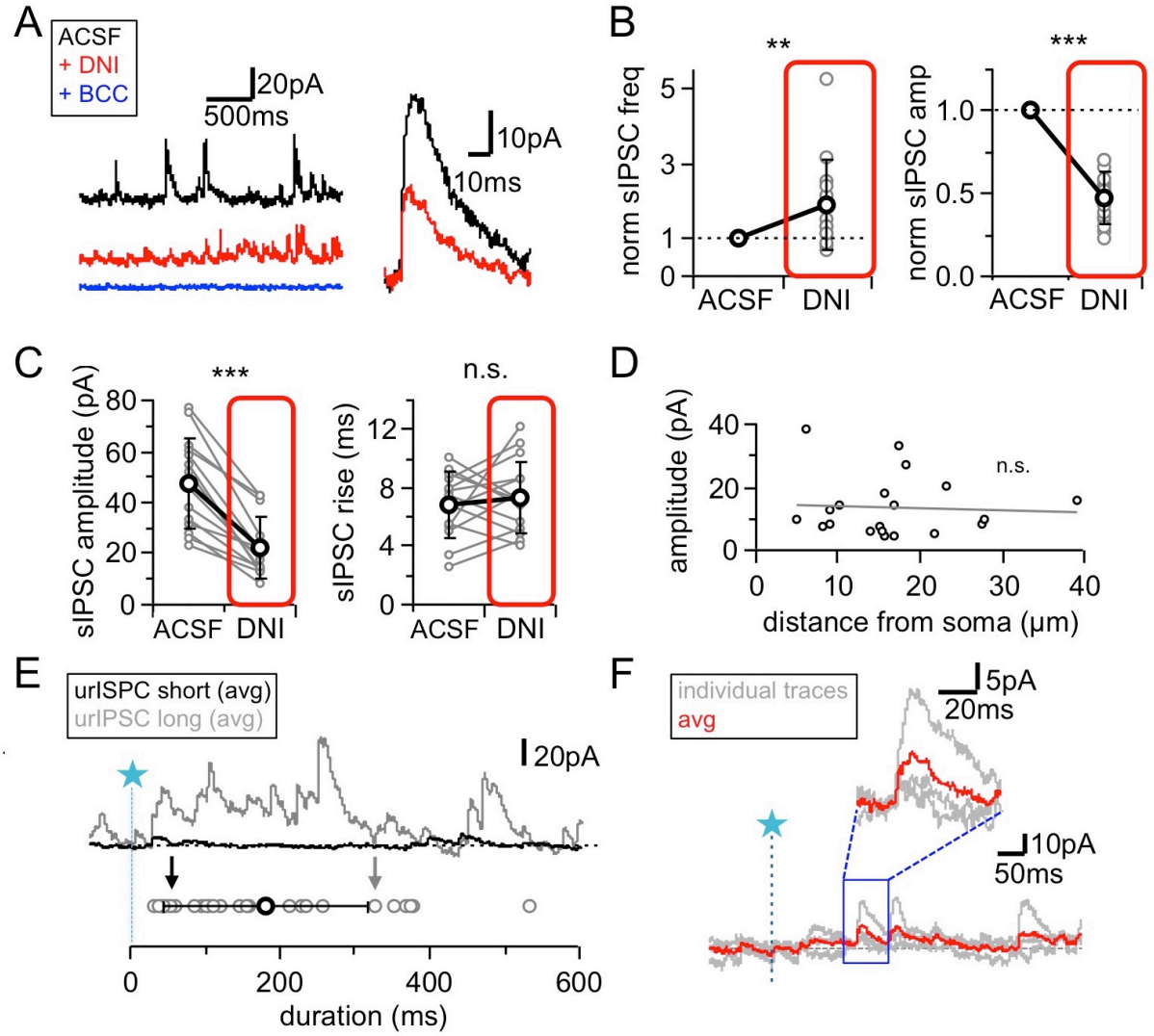

Figure S1. Effects of DNI (1 mM) on sIPSCs, uncaging sites, duration of responses
(**A**) Left: Example recordings in ACSF, after DNI wash-in and with added bicuculline (BCC, 50 µM). Right: Representative single events before and after DNI wash-in.
(**B**) Summary of effects of DNI (red) on spontaneous IPSCs. Left: Amplitude Right: Frequency (n = 14 MCs).
(**C**) Absolute changes in sIPSC parameters (amplitude, rise time) upon wash-in of DNI (red, n = 14).
(**D**) Distance of TPU site from soma versus urIPSC amplitudes. No correlation was found (n = 20).
(**E**) Top: Exemplary averaged responses from two experiments. Bottom: Cumulative durations of triggered events (black and grey arrow: durations of exemplary averaged responses).
(**F**) Exemplary experiment with a long latency of first detectable response (see Methods). Inset: Magnification of responses.